Delft University of Technology

Master's Thesis
MS53035

Wire-based Laser Metal Deposition of Aluminium Alloys

Authors:
Hsiao-Hsuan Teng (5930448)

Date of Defence:
11th December, 2025

Contents

Abstract

Wire-based laser directed energy deposition (LDED) using wire feedstock offers a promising path for fabricating medium- to large-scale structures, yet the process remains highly sensitive to both process and material conditions.

This work investigates the relationship between process parameters, microstructure, and defect formation in single-bead and multi-layer depositions of aluminium 5356 alloy, with a particular focus on understanding the evolution of bead geometry, porosity, and distortion under different processing conditions.

Single-bead experiments were conducted to explore the individual effects of key process parameters (laser power, travel speed, and wire-feeding rate) on deposition stability. The results showed that bead geometry followed predictable trends dependent on heat input and the amount of feedstock, enabling the definition of a workable processing window for further vertical builds. Although clear microstructural trends were not observed in single tracks, compositional variations at the deposition-substrate mixing area indicated local dilution effects that may influence grain morphology during the first-layer solidification.

Multi-layer depositions demonstrated the characteristic microstructural features of DED processes, including directional columnar grains and finer equiaxed dendrites, reflecting the thermal gradients and cooling conditions during the build. Defect characterisation revealed that porosity systematically increased with both layer number and travel speed. These trends are consistent with shorter melt pool lifetimes limiting gas escape. The pore morphology confirmed the predominance of gas-induced pores; combined with the absence of measurable magnesium loss, hydrogen from the feedstock remains the most likely dominant source. Thermal distortion was observed to escalate with both build height and heat input, underscoring the sensitivity of thin-wall geometries to thermal accumulation.

Overall, this study provides experimentally based insights into parameter–process interactions in wire-based LDED of aluminium alloys. The findings help clarify processing limits for thin-wall geometries, identify critical sources of defect formation, and highlight future opportunities for improving process stability through better thermal management and more precise process control.

Acknowledgements

I would like to take a moment to express my deepest gratitude to all the people who have supported and helped me during my master's studies, especially in my thesis work.

I would first like to express my gratitude to my supervisor Dr. Marcel Hermans, for his guidance, support, and encouragement throughout the thesis project. His kindness and feedback have shaped my growth as a researcher.

I am deeply thankful to Dr. Arjun Sood. I truly appreciate the time he dedicated to helping me, as well as his patience and willingness to discuss every detail with me.

My thanks also go to Jurriaan van Slingerland for his experience and insights with the laser equipment. I would also like to thank DP Sharma Mainali for his assistance in the laboratory and for his constant availability. Their technical support made this research possible.

The gratitude also extends to all the people I have met but couldn't name in this country. To me, it's "iân-hūn" that binds us together. Call it what you want, fate or serendipity, since there's no translation for it.

Then, I am so deeply indebted to my family, literally. I would like to thank my parents for their support, especially financially, throughout my studies. To me, gratitude always comes with guilt. So, it's also a sorry to them, for me being "thó-tsè" and "khioh-kak".

Finally, I would like to thank my friends: Ning, sorry I have to be part of the "comes and goes" of yours, but I have witnessed your strength and believe you will manage regardless. Jessica, to me, you are the personification of "wrath". And this burning wrath of yours is something that keeps me from drifting away. Grenache, I still like calling you by this name. Thank you for the endless companionship and tolerance of my complaints. Rosie, my sibling-like dear friend, I always appreciate your version of "caring". I cherish the moments we have shared across time and space, with cigarettes. Li-Hsuan, as I said before, you have always been the constant of my life, an anchor. I must be lucky to find both friend and family in you.

In the end, this part may seem pretentious, but I wear everything on my sleeve. To my fellow islanders, thank you for defending our country and democracy. The path of our nation will only continue, and thus our fights. There's something I want to say and will only sound beautiful in my own language: "Chū-iû Tâi-oân, tok-lip kiàn-kok". An oath, a promise, a spell, a wish, and a future we all fight for.

Hsiao-Hsuan Teng
Delft, December 2025

List of Figures

List of Tables

Chapter 1

Introduction

Additive Manufacturing (AM) technology, known as 3D printing, is a process that directly manufactures products layer by layer according to computer-aided design (CAD). Its layer-by-layer fabrication is unlike conventional subtractive manufacturing, allowing the production of geometries that would otherwise be difficult to machine. AM has become an increasingly important approach for producing near-net-shape components with reduced material waste, shorter manufacturing cycles, and increased design flexibility. Many metal-based AM processes share significant similarities with welding techniques. In general, it involves the formation of a fusion zone with liquid metal that moves along with a moving heat source and then solidifies into the desired shape. Although, unlike welding, where solid metal surrounds the fusion zone on both sides, AM processes do not exhibit this characteristic. What distinguishes AM is the repeated deposition and reheating of material, the continuously evolving geometry, and the strong dependence of the final part quality on thermal history.

It has gained significant attention in industrial applications due to its ability and versatility to create complex shapes with decent accuracy. AM processes also exhibit flexibility in material selection, allowing the manufacturing of a variety of materials, such as metals, polymers, ceramics, etc. With significant advantages compared with conventional manufacturing methods, many new AM processes have been developed and successfully applied in countless fields. In the AM process, variations in feedstock materials and the heating source further differentiate these processes, each possessing distinct advantages. Other critical aspects of AM include the interaction between the heat source and feedstock material, the sequential layering of deposited material, repeated thermal cycling at specific locations as new layers build upon previous ones, and transient geometric changes, all collectively play a crucial role in understanding AM.

Among the wide range of metal AM techniques, laser-based processes have gained particular attention. Incorporating lasers as the energy source in AM exhibits several advantages, including the ability to manufacture complex components and tiny features due to the fine laser beams, enabling high precision and high-resolution manufacturing. Additionally, the use of a laser enables highly localised heating and rapid cooling, which directly influence the solidification behaviour and result in grain refinement of the deposited material due to its high energy density[1].

Laser directed energy deposition (LDED), also known as laser metal deposition (LMD), is one such technique that enables the fabrication of near-net-shape structures, component repair, and the integration of features onto existing substrates. As a branch of the broad AM technology, LDED employs a laser as the energy source and is largely used for the deposition of high-performance materials and is used in aerospace, automotive, biomedicine, etc. In LDED, metallic feedstock is introduced into a laser-generated melt pool and solidifies as the heat source travels. In general, LDED processes can be classified into two main types based on the feedstock selection. Typically, metals and alloys can be prepared in the form of powder or wire as feedstock. While both forms rely on the same fundamental laser–material interaction, wire-based LDED offers several practical advantages, including higher material efficiency, reduced contamination risks and simpler feedstock handling. These characteristics make wire-based LDED especially attractive for structural materials where material cleanliness and consistency are critical.

Aluminium alloys have long been regarded as promising candidates for LDED, supported by their high strength-to-weight ratio, favourable properties and extensive industrial use. However, processing of aluminium alloys through wire-based LDED remains challenging. The high thermal conductivity, low absorptivity to lasers and strong tendency toward defect formation, particularly porosity, lead to complex behaviour during deposition and an elevated susceptibility to defects. These factors influence process stability, defect formation, and the resulting microstructure, making controlled deposition difficult. As a result, establishing stable deposition conditions for aluminium alloys and understanding the mechanisms that govern defect formation and

microstructural evolution remain active areas of research. Although a wide variety of works have been carried out on powder-based aluminium deposition, fewer studies have focused on wire-based systems. Variations in heat input, travel speed, wire-feeding rate, and process stability can strongly influence deposition shape, interlayer bonding, thermal accumulation, and the development of defects. A clearer understanding of the relationships between process and build is therefore important for defining processing windows, improving build stability, and informing future modelling and optimisation strategies.

This thesis work aims to provide a systematic experimental investigation of the deposition behaviour of aluminium 5356 wire produced by wire-based LDED, focusing on both single-bead and multi-layer depositions. Through combined geometrical, microstructural and defect-oriented analyses, the work aims to contribute to a more systematic understanding of the overall build characteristics of wire-based LDED of aluminium alloys.

The remainder of this thesis is structured as follows: Chapter 2 builds on the theoretical backgrounds and reviews the principles of LDED and the challenges associated with aluminium alloys in the processes. Chapter 3 describes the experimental setups and characterisation methods. Chapter 4 presents results from single-bead and multi-layer experiments, while the interpretations and implications of the findings will be carried on in Chapter 5. At the end, the discussion is followed by conclusions and recommendations in Chapter 7.

Chapter 2

Theoretical Background and Literature Review

2.1 Theoretical Background

This section describes the fundamental knowledge related to the topic of this thesis. The laser metal deposition process is introduced, followed by the details on the aluminium alloys. The common defects and issues encountered in the processes of LDED in general and of aluminium alloys in particular are also included in the latter section.

2.1.1 Laser Direct Energy Deposition

Laser Direct Energy Deposition (LDED), also known as Laser Metal Deposition (LMD), involves high-energy density sources to focus on the substrate, forming a melt pool and melting the feedstock material placed into the melt pool at the same time. When the heating source moves according to the designed route of the scanning strategy, the deposited metal quickly solidifies into a layer on the substrate, forming a track. Then, the energy source is lifted to a preset distance to deposit the next layer, subsequent tracks overlap each other with a certain hatch spacing, and the process repeats layer-by-layer after the previous one is finished. Eventually, a three-dimensional structure can be formed by multi-layer deposition[2].

Different energy sources can be adopted in DED processes, such as an electric arc, an electron beam, or a laser. Being a branch under Laser Additive Manufacturing(LAM) processes, LDED is largely used for the deposition of high-performance materials and is used in aerospace, automotive, biomedicine, etc.

LDED technology has gained widespread attention due to its numerous advantages. The main benefits include its cost-effectiveness, less material consumption, high deposition rate, superior adaptability to materials, flexibility of automation and integration[2], and a relatively wide process window compared with other metal AM methods[3]. The metallurgical bond formed between the deposited layer and the substrate also gives high interface strength[2]. Additionally, the utilisation of a laser results in more benefits. The small laser spot diameter and fast scanning speed lead to the low dilution rate in the process, thus improving the properties of the substrate and the deposition[2]. Moreover, the heat-affected zone (HAZ) of the process is relatively small, making it ideal for the repairs of high-value components[4]. It has been reported that there were successful repairs of damaged components that are difficult to process in conventional methods without forming a weak heat-affected zone or the introduction of cracks[5].

In general, LDED processes can be classified into two main types on the basis of the feedstock selection. Typically, metals and alloys can be prepared in the form of powder or wire as feedstock. Powder-based processes generally have longer production times due to limitations such as feeding rates, scanning speeds, and low layer thickness. In contrast, wire-based approaches offer a higher material deposition rate, as wires enable greater mass flow. As a result, powder-based processes are better suited for fabricating smaller, high-precision components, whereas wire-based methods are preferred for manufacturing larger-scale structures[6].

One key distinction between these approaches is the post-processing requirement. On the one hand, wire-based AM fabricated parts often require further machining to achieve the final ideal shape because of the larger melt pool and bead formation during deposition. On the other hand, powder-based AM methods typically form near-net-shape components with fine details, reducing the need for additional finishing.

Wires are relatively cheap compared to powders of the same alloy as different types of alloys are manufactured by wire drawing. However, despite the lower cost of wire feedstock, the material waste generated during

machining can offset these cost savings. Wire selection presents challenges; commercially available welding wires used in AM tend to produce larger melt pools than powder-based processes, leading to less-fine surface finishes[7].

While both deposition methods possess their advantages and shortcomings, wire-based systems offer key advantages over powder-based ones. It has a significantly lower surface area per kilogram compared to powder, making it less susceptible to oxidation, moisture, and contamination. Additionally, wires are easier to store, handle, and transport, posing fewer environmental, safety, and health risks compared to metal powders.

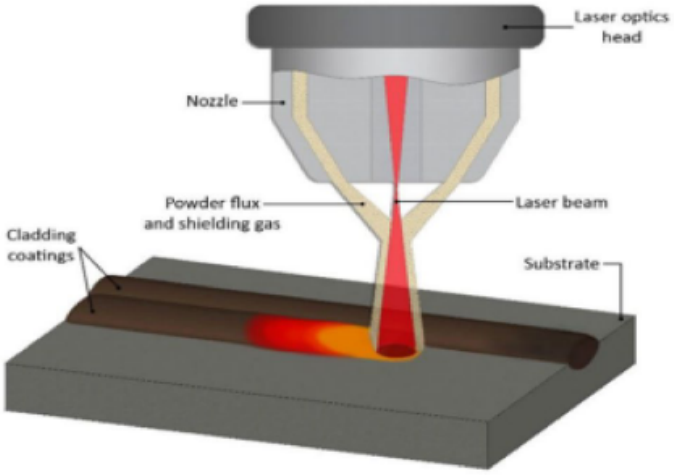

Figure 2.1: Diagram of the powder-feed system LAM technology[8].

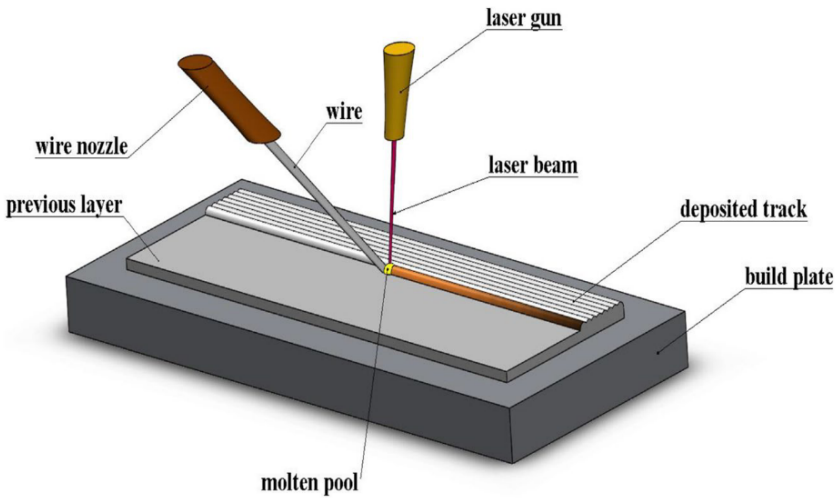

Figure 2.2: Diagram of the wire-feed system LAM technology[8].

2.1.2 Laser

1. **Laser-Material Interaction**
   Laser absorption in a metal depends on various conditions, involving both the laser and the metal. Nevertheless, the reflectivity of a metal surface depends greatly on the wavelength of the light incident, the angle of incidence, the surface roughness, the presence of surface films or oxide layers, the composition of the material and even temperatures. Reflection, transmission and absorption happen when light contacts the metallic surface. To ensure an efficient laser process, as much incident laser energy on the workpiece has to be taken into account; thus, absorptivity is essential to understand. Absorptivity is defined as the ratio between absorbed energy and the incident energy[9]. The laser absorptivity has a tendency to

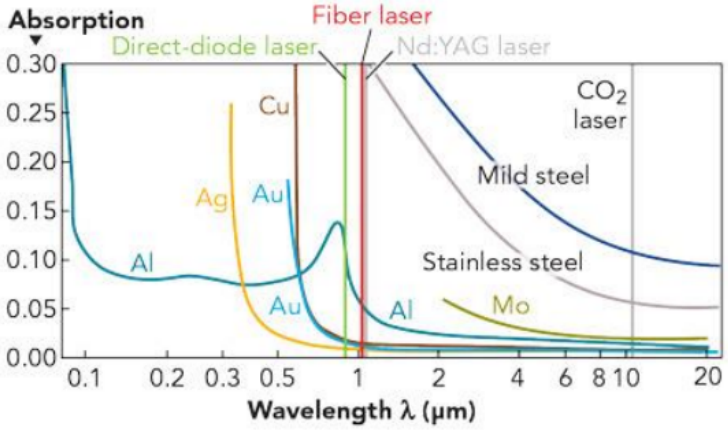

Figure 2.3: Radiation of laser absorbed varies the wavelength for different metals[10].

decrease with increasing wavelengths, as shown in Figure 2.3. In the figure, aluminium shows a relatively lower absorption rate to the commonly used laser types marked in the figure.

2. **Laser Operation Modes**
   Typically, laser operation can be conducted in two different modes: **thermal conduction welding** and **keyhole welding**. Figure 2.4 gives a schematic view of the two laser operation modes. The two different modes depend on the power density of the laser beam at the work surface and the resulting temperature distribution.

   - **Conduction mode:**
     In conduction modes, the heat is primarily distributed inward through thermal conduction, as shown in Figure 3 (a). This mode usually happens at lower power densities, typically below 10^5 W/cm^2[11]. In the conduction mode, no significant material vaporisation occurs since the temperature remains below the material's evaporation point, leading to a shallower penetration of the melt pool. This results in a stable process with high reproducibility and a smooth weld surface. However, conduction welding is generally inefficient for bulk metals due to high reflected and dissipated energy loss, limiting penetration depth.
   - **Keyhole mode:**
     In keyhole mode laser welding, the temperature is elevated sufficiently for surface evaporation to happen, the power density required for the keyhole mode is dependent on the alloy types. This generates recoil pressure, which in turn causes the molten zone depression, see Figure 2.4 (b). The term "keyhole" originally referred to the presence of a hole completely penetrating the workpiece created by the heat source in a welding process; it now refers to any process with a deep cavity, regardless of full or partial penetration. Unlike conduction welding, where heat spreads primarily through conduction, keyhole welding allows the laser energy to penetrate deeper into the material. Multiple reflections of laser irradiation inside the keyhole enhance absorption efficiency, enabling direct heating of regions below the original surface. This mechanism enables the formation of high-aspect-ratio welds, making keyhole welding advantageous for deep penetration applications.

3. **Laser Spot Size**
   The laser beam irradiance indicates the applied energy density within a given focal spot area, defined as the power per unit area. Froend et al.'s investigation suggested that the laser beam irradiance can be used in obtaining different microstructures while maintaining the constant heat input by adjusting the focal spot area.

$$I = \frac{P}{A} \tag{2.1}$$

In order to obtain the maximum efficiency, the spot diameter in laser welding processes is usually adjusted. On one hand, a finer spot size and a thinner layer combined with proper processing conditions is able to meet the requirements of high-precision products, but the time required for its production will increase. On the other hand, a larger spot size with a thicker layer improve the production efficiency. In wire-based

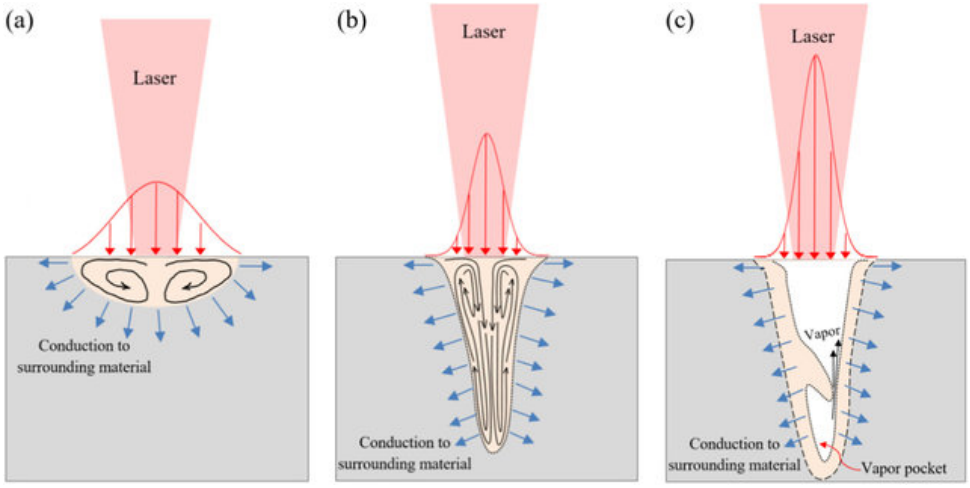

Figure 2.4: Melt pool formation mechanisms a) conduction mode b) keyhole mode c) keyhole with porosity[12].

LDED, where the wire diameter taken into account, the focal spot diameters are adjusted to ensure the coverage of the entire wire. But a fraction of the substrate surface needs to be captured by the laser spot area, promoting a stable melting process.

In the wire-feeding systems, it is essential to align and adjust the distance between the laser focal point and the melt pool vertically. In order to obtain a stable process, maintaining a nominal focal distance with other constant process parameters is the key.

In most of the studies in LDED processing, a defocus distance is usually set during the processes. To achieve the defocusing of the laser, it could be either altering the laser head in the Z-direction to increase the focal spot size. The spot size increases when the defocus distance increases away from the beam convergence plane, which in turn lowers the local energy density.

At low focal positions, the laser beam area on the substrate is too large, meaning the beam has a lower intensity. Consequently, the wire collides with the substrate and could fail to melt uniformly due to insufficient energy received.

It was found in the previous work[13] that to effectively control the intensity and heat input of the energy source for solving common issues, a negative defocusing of the laser can be applied. This adjustment provides a mechanism that allows the modification of the distribution of heat between the feedstock and the substrate, further influencing the deposition geometry obtained.

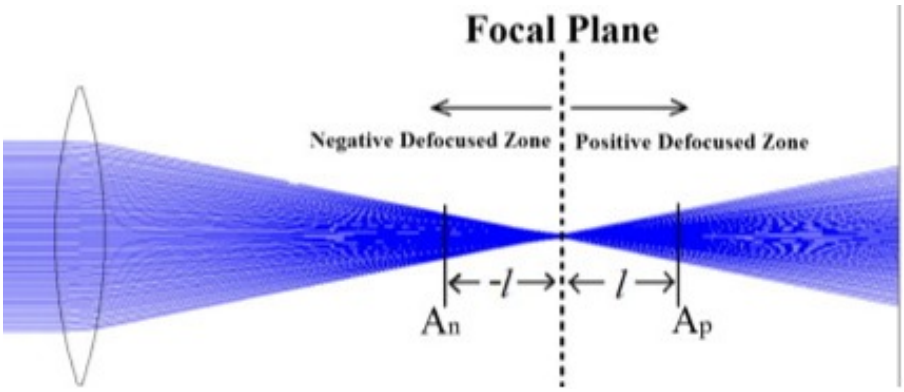

Figure 2.5: Simulated scheme of ray diagram of a parallel Gaussian laser beam through a focusing lens[13].

In order to obtain a consistent laser spot size throughout multi-layer processes, a specific height increment must be applied with each successive layer. This increment determines the vertical shift of the process plane and directly affects layer alignment.

When using a height increment smaller than the calculated value, it results in a measured part height greater than expected. In contrast, when a height increment larger than the calculated value is applied, it

leads to a measured height lower than predicted. In both cases, the height increments used deviate from the theoretically calculated value; the deposition of consecutive layers would ultimately lead to a process failure due to the mismatch between the actual part height and the adjusted height of the process plane.

If the theoretically calculated height increment is used, the final height of the produced part closely matches the intended process height, particularly at lower speed ratios. However, larger deviations occur at higher speed ratios, especially for aluminium alloys.

2.1.3 Aluminium alloys

Aluminium alloys are broadly used in industries with high demand for performance due to their desired properties like low specific weight, better corrosion resistance, specific strength, and high thermal conductivity. In the LDED processes of fabricating metal components, the exploration and interest in aluminium alloys with different compositions and alloying elements has grown in recent years because it is made possible to create structural parts at lower cost and higher efficiency.

Aluminium alloys are classified into different series based on their composition and strengthening mechanisms. Typically, aluminium alloys are classified as wrought or cast based on composition. Cast aluminium alloys typically contain 10–12% alloying elements, whereas wrought aluminium alloys have a lower alloy content, ranging from 1–2%[14].

The 1000-, 3000-, 4000-, and 5000-series are non-heat-treatable and rely on solid solution strengthening or mechanical deformation for improved properties. In contrast, heat-treatable alloys, including the 2000-, 6000-, and 7000-series, achieve enhanced strength through heat treatment processes. The 8000-series, which incorporates various other elements, is primarily used for aluminium foil, while the rarely utilised 9000-series serves as a reserve classification[14].

Among several series of aluminium, the 5000-series alloys primarily contain magnesium as the main alloying element, typically with small amounts of manganese for dispersion strengthening[15], and alloying element percentages vary from 3 to 6%[16]. The addition of magnesium in this series results in properties like high strength, better weldability and corrosion resistance. And because of their properties, 5000-series alloys are commonly applied in the aerospace industry and maritime components.

In general, aluminium has numerous advantages, such as corrosion resistance, lightweight characteristics due to its low density, and high specific but a relatively low Young's modulus. Additionally, they are easily shaped because of their FCC lattice structures. However, the inherent characteristics of Al alloys are still considered challenging when they are fabricated with the LAM process. Considering the positive features of aluminium, it is equivalently necessary to highlight the challenges in handling aluminium and how to overcome them in the process.

- **Absorption**
  To begin with, the high reflectivity and thermal conductivity of aluminium to laser may lead to the requirements for higher laser power to achieve proper melting in the processes. Metals have different absorption rates for different wavelengths, thus the laser energy. As suggested in Figure 2.3, the laser energy is partially absorbed by the material as the laser interacts with the melt pool. Hence, the energy efficiency and material deposition rate in the process are directly influenced by the different laser absorption of each material[1]. Aluminium shows a low absorption rate for longer wavelengths. Therefore, aluminium alloys in the LAM process usually need higher laser power. The use of higher energy input will induce the vaporisation of alloying elements with lower boiling points, such as Zn and Mg.

- **Oxidation**
  In general, aluminium is prone to oxidation. Therefore, in realistic cases, aluminium is often coated with an oxide layer. Aluminium oxide (alumina) layers appear on the surface of aluminium alloys, which may diminish the laser absorbance of the material. Alumina layer is transparent but has a high refractive index, n =1.62 for a wavelength of 0.78 m[17]. The presence of oxide layers affect the reflectivity. Aluminium has a high reflectivity while alumina appears partially transparent, so the absorbance and reflectance are different, depending on the thickness of the alumina layer[18]. Therefore, the laser interacts with the oxide layer, partially reflected before reaching the underlying aluminium surface, resulting in a decrease in the overall absorption efficiency of the material[19]. The oxide layer also can hinder the bonding between newly deposited material and solidified material, compromising the build efficiency and density.

  Because of the interactions between aluminium and oxygen at relatively low temperatures, the surrounding environment conditions are important in aluminium alloy processing. Control of the atmosphere, specifically oxygen content, is usually required to achieve target properties by avoiding the formation of

aluminium oxides. Aluminium oxides generally have higher melting points, affecting the wettability and leaving oxide inclusions and pores in the materials deposited.

- **Vaporisation of Alloying Elements**
  In the processing of steels and non-ferrous alloys, the loss of volatile alloying elements commonly happens[20], remaining one of the key challenges. Aluminium alloys are prone to the evaporation of elements with lower boiling points when processed at high temperatures. Particularly, they are known to lose magnesium and zinc[21]. As discussed in the previous section, due to the requirement for higher laser power for aluminium in LAM processes, it usually results in significant vaporisation of alloying elements. The losses have a negative influence on the final material properties, based on changes in microstructure, compromising mechanical performance and corrosion resistance[20]. Therefore, process control and parameter optimisation are crucial to minimise the undesirable effects.

2.1.4 Defects in LDED Processes

1. **Distortion**
   In general, distortion is a usual and inevitable phenomenon in the layer-by-layer processes in additive manufacturing. Owing to the high energy input used in LDED processes, the workpieces usually involve melting, reheating and remelting. Hence, they experience frequent heating cycles and have a complex thermal history due to the high-intensity energy source. The localised heating from the moving laser and the non-uniform cooling in the process result in large thermal gradients[22]. This, in turn, will result in rapid non-equilibrium solidification[23]. The rapid cooling and the thermal gradients of the workpiece lead to residual stresses and thus the distortion in the components, further resulting in intricate phase transformations and microstructural changes[24].

   The complex thermal history of the fabricated parts using LDED is affected by numerous processing factors, all control the temperature history and solidification of the deposit and significantly affect the microstructure, properties, and characteristics of the material as-deposited.

   The distortion values can vary in the samples, which is linked to how the residual stresses developed in the workpieces. The distribution of the residual stresses results from the thermal cycling from the laser processing in the layer-by-layer development. A temperature gradient exists between the bottom and each new layer subsequently deposited.

   Residual stresses and distortions in the fabricated components diminish the mechanical performance and geometrical accuracy; thus, the mitigation of both is essential in ensuring the quality. These are two key challenges that severely limit the application and development of LDED technology. All thermomechanical manufacturing process leads to the formation of residual stresses. Therefore, understanding the thermomechanical behaviour involved in the process is crucial for the mitigation strategies.

   In Figure 2.6, the potential reasons for residual stresses and distortion in the deposited structure stem from the shrinkage occurring in the deposited material. With the localised heating from the laser, a significant thermal gradient happens, and compressive stress builds up in the workpiece. When the compressive stress exceeds the material's yield strength, plastic deformation occurs in the heat-affected zone, resulting in the upward bending of the workpiece. And during the cooling, the same region experiences thermal contraction. At the same time, the existing plastic strain resists the contraction, inducing tensile stress that causes the workpiece to bend downwards. The deposited material experiences contraction during solidification, causing a shrinkage in volume. Afterwards, due to the bonding between the substrate material and the deposited layer, compressive stresses then occur in the substrate, whereas the deposited layer experiences tensile stresses. A similar phenomenon also happens when a subsequent layer of material is deposited. These stresses pile up and can eventually induce further distortion of the structure.

2. **Porosity**
   The pore formation during the process is one of the common defects that significantly influences the quality of formed parts by LAM and has been at the centre of attention for various fields. The porosity lowers the overall density of the deposition and, in turn, compromises the mechanical properties of the fabricated parts. The existence of pores is an inevitable issue to be controlled or mitigated to avoid the influence on the mechanical properties[26]. The number, size, and position of the pores collectively contribute to affecting the properties of the components, and the effect of them on mechanical properties is related to their size and shape[27]. For instance, the presence of irregular pores has a higher possibility of acting as stress concentrators in the components.

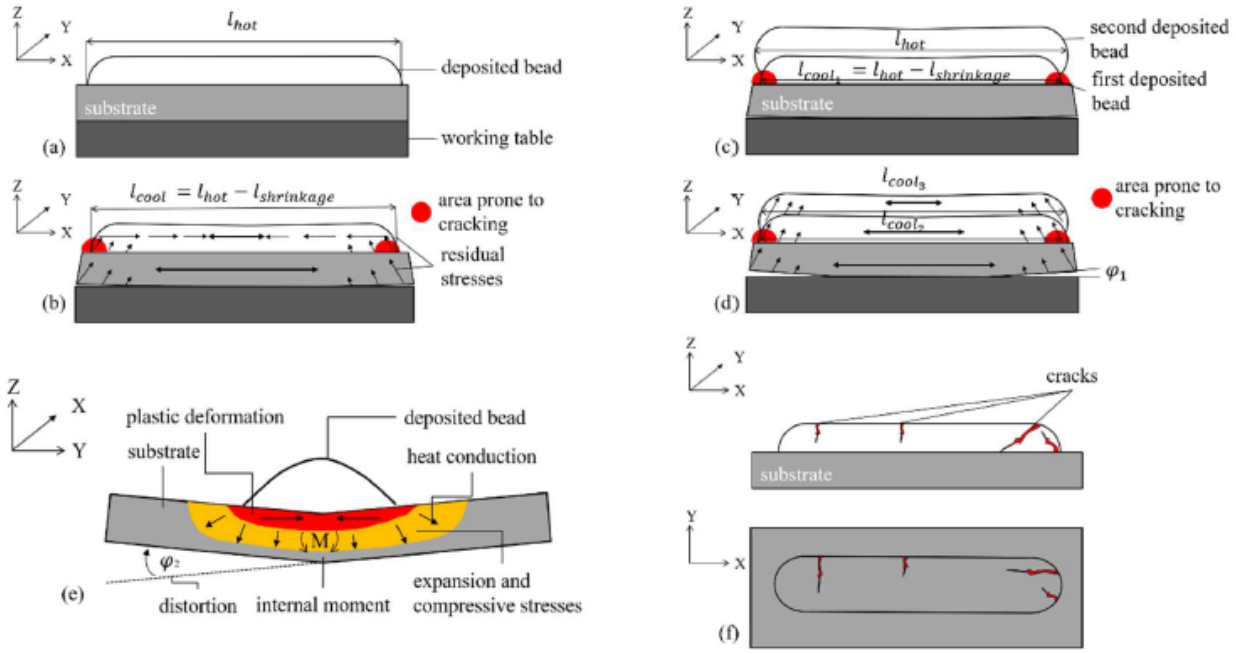

Figure 2.6: Schematic visualisation of a deposited bead with a length of l_{hot} (a) and its shrinkage while cooling down, inducing residual stresses and deformations of the substrate for a single bead deposition (b) and (e). As well as multiple layer LMD with bead lengths of l_{hot} due to subsequent deposition (c) and cooled down state, which leads to residual stresses in both layers and the substrate (d). Additionally, cracking within the bead is visualised (f) [25].

Hydrogen is one of the primary sources of pores in the processing of aluminium alloys. The significant difference in the hydrogen solubility of liquid aluminium and solid aluminium contributes to the pore formation in aluminium. Specifically, 0.65 and 0.034 mL/100 g for liquid and solid, respectively[27]. When the aluminium alloy experiences the transition of solid and liquid phase, the hydrogen atoms begin to precipitate out of the solid phase and move to the liquid phase. The hydrogen in the liquid phase then starts to accumulate, and when exceeding the solubility of the liquid phase, hydrogen atoms combine and form gas molecules. This phenomenon is especially pronounced in LDED processes, as the high solidification rate limits the time for releasing the hydrogen gas molecules.

In welding and AM processes, the main source of the hydrogen comes from the wire itself. The presence of hydrogen emerges in aluminium wires mainly because of the moisture, grease, and hydrocarbon contaminants on the surface. In addition, it is reported that pore formation from hydrogen is more difficult to control in AM processes due to the amount of the wires being used[28].

Aside from hydrogen, pores can be process-related, mainly caused by the entrapment of the vapours coming from shielding gas or air failing to escape. Due to the high conductivity of aluminium, the solidification is rapid, leaving less time for the vapours to escape from the melt.

Considering process conditions, laser power and scanning speed are the key factors in porosity and other defects. Porosity can be mitigated by elevating the power or reducing scanning speed as it gives a longer solidification time for the gases to escape, but it also leads to a higher possibility of hot cracking regarding alloys sensitive to hot cracking[29]. Aside from laser power and scan speed, hatch spacing also plays a key role in the formation of pores because it affects the fusion of the materials[30]. Insufficient overlap between scan tracks may happen with the increase of hatch spacing, causing more pores in the fabricated parts.

- **Metallurgical Pores**
  Metallurgical pores are entrapped gases in the molten pool when solidifying. The high solidification rate of the process leaves not enough time for the gases inside the pool to escape, hence the formation of pores. The gases can originate from the feedstock, potentially an element selectively evaporated from the alloy during the heating process[31].

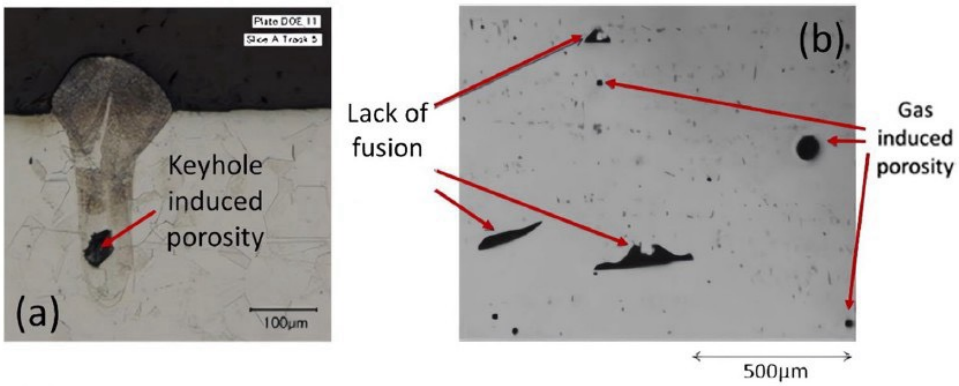

Figure 2.7: (a) Defect of keyhole-induced porosity; (b) Defect of lack of fusion and gas-induced porosity[33].

Pores formed by gases are usually in spherical shape and have the smallest size among all pores. It is found that this type of pore can only be reduced, but cannot be eliminated[32].

- **Keyhole Pores**
  Keyhole pores are induced when high-energy input is adopted and localised vapourisation happens. When the energy density is elevated, the melting mode transforms into keyhole mode, as shown in Figure 2.7. The keyhole mode melting is a vapour depression phenomenon, also well-known in welding. As the energy input increases, the molten pool goes through a transition from a shallow semi-elliptical shape to a narrow and deep, valley-like shape. The metal vapour may be entrapped at the tip of the keyhole in the melt pool and form keyhole pores in keyhole mode[32]. Keyhole pores can vary in shapes, generally with the size of 10 to 50 μm.

  The keyhole pores by entrapped metal vapour can be differentiated from metallurgical pores because they can be eliminated by lowering the energy density to stabilise the melting mode. However, the metallurgical pores can never be completely eliminated as discussed in the previous section[32].

3. **Microstructural Evolution**
   The properties of metals are closely linked to their microstructure. In laser-based additive manufacturing, a complex transformation is involved because of rapid solidification and repeated thermal cycles. The transformation is influenced by the collective effect of laser energy, heat, and material behaviour[34]. The melting and solidification process directly affects local microstructural characteristics, including grain morphology, size, and crystallographic texture[35]. During solidification, the morphology of the grain structures plays a crucial role in shaping the final properties of the deposited parts[2].

   The solidified grain morphology is primarily affected by heat conduction (temperature gradient, G) and mass transfer kinetics (solidification rate, R). The cooling rate, given by the product $G \times R$ [K/s], dictates the size of grains, i.e. fineness of the microstructure. With higher cooling rates, it leads to finer structures due to the reduced diffusion length during solidification. On the other hand, the ratio G/R [Ks/m^2] determines the stability of the solidification front and governs the resulting interface morphology, which can be planar, cellular, or dendritic. As suggested in Figure 2.8, lower G/R values generate equiaxed dendritic structures, while higher values typically lead to columnar dendritic structures[15]. By carefully controlling the G/R ratio, the grain structure can be tailored to achieve the desired material properties.

   Typically, there are two main solidification mechanisms within the melt pool taking place in laser melting deposition heterogeneous nucleation for equiaxed grains and epitaxial growth for columnar grains. The two mechanisms compete with each other, dominating the grain morphology selection process and collectively defining the solidified grain morphology[5].

   The morphology of metal crystals in the cladded layer is mainly equiaxed grain and columnar grain. On the upper part near the surface, where the temperature is higher, the main composition are fine, smaller equiaxed grains since the probability of grain nuleation is approximately equal. On the other hand, on the lower part of the deposited layer, mainly forms coarse, larger columnar grains.

   Equiaxed grains are smaller-sized and isotropic, thus present more uniform mechanical properties. Conversely, columnar grain structures are coarse and appear to have fibrous textures[37]. Certain directions of aligned columnar grains lead to undesired anisotropy of mechanical properties. The dendrites of the columnar grains usually grow along the direction perpendicular to the substrate and closest to the direction

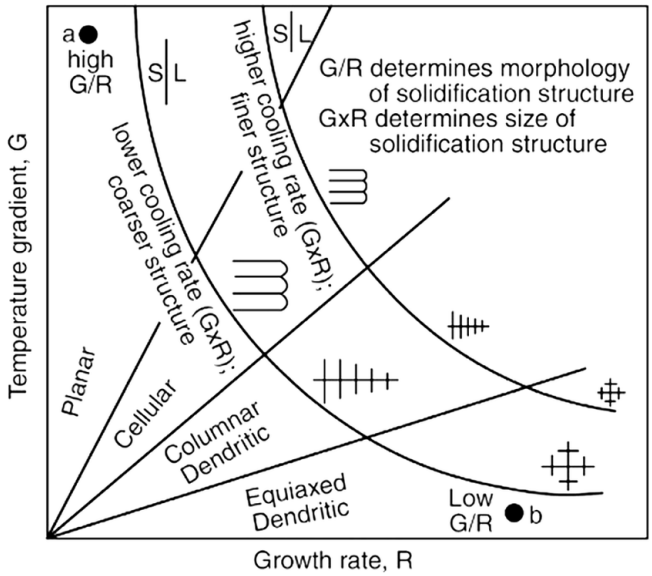

Figure 2.8: Effect of temperature gradient (G) and growth rate (R) on the morphology and size of solidification microstructure [36].

of the heat flow[38]. The anisotropy in mechanical properties is specifically harmful to applications experiencing multidirectional stresses[39]. Additionally, columnar grains generally have more grain boundaries in the build direction, leading to a higher probability of cracking.

2.2 Key Influential Factor Identification

In the processes of wire-based laser metal deposition, a wide range of process parameters influences the stability of the melt pool, deposition geometry, defect formation, microstructure and more. These parameters can generally be grouped into three categories: laser-related parameters (e.g. power, spot size, mode), wire-feeding-related parameters (e.g. feed rate, wire angle), and deposition-related parameters (e.g. travel speed, shielding gas, overlap strategy). While many of these parameters interact and affect the process in complex ways, a review of the literature indicates that a narrower subset gives the most direct influence on whether deposition is successful or prone to defects. Attempting to treat all possible variables equally would not only be impractical but would also obscure the main controlling factors.

- **Laser Power**
  As the main source of power, the appropriate laser power is crucial in determining the amount of energy each point takes locally. It is closely related to the amount of feedstock material being melted and how much the substrate is heated. Inadequate laser energy densities may result in not fully melting the feedstock materials, leading to a lack of fusion or adhesion problems between layers.

  In addition, a turbulent flow could be induced by high energy density and in turn absorb shielding gas, resulting in pore formations. A high energy density might also result in more pronunced evaporation. As mentioned in the earlier section, keyhole modes can also be induced in excessive energy densities, which will cause keyhole pores to form. Therefore, considering the laser welding modes, the laser energy is suggested not to exceed the threshold for causing the keyhole modes.

  Several different indicators are used to characterise energy input. For instance, there are linear energy density, areal energy density, volumetric energy density, laser irradiance and specific energy. Among the indicators, except for specific energy, others are based on the laser spot size or focal spot area.

- **Travel Speed and Wire-Feeding Rate**
  Travel speed and wire-feeding rate collectively decide the amount of wire being melted. Despite that travel speed and wire-feeding rate are each from different groups, the two have to be considered. Since the travel speed and wire-feeding rate are interrelated with each other, speed ratio, or k-value, defined as Equation, are used to correlate the two in the literature.

  The deposition rate is related to the wire diameter, the density of the wire material and the wire-feeding rate, as defined in Equation 2.2. When using a constant wire material and diameter, both ρ and r remain

fixed. As a result, the deposition rate is directly proportional to the wire-feeding speed, making WFS the only variable influencing the deposition rate. Since deposition rate ultimately reflects the actual material buildup during the process, it serves as a more meaningful parameter for evaluating process performance and material efficiency than wire-feeding speed alone. Therefore, it is more appropriate to consider deposition rate when comparing process conditions or assessing productivity.

$$\dot{m} = (\text{WFS}) \cdot \pi r^2 \rho \tag{2.2}$$

The deposition rate, along with the laser power, collectively influences the resultant deposition and process efficiency. It is suggested that merely raising the deposition rate without altering the laser power will lead to partial melting of the feedstock material. Therefore, with the understanding of the relation between the wire-feeding rate and laser power, the limits of the wire feeding rate based on given laser power inputs can be established[40].

To regulate the deposition rate, an indicator, speed ratio or k-value (see Equation 2.3), is used to correlate the wire-feeding rate and the travel speed, referring to the ratio between the two. This indicator has been used to evaluate how various process parameters affect the defect formation during the deposition process.

$$\textit{Speed Ratio} = \text{WFS/TS} \tag{2.3}$$

- **Height Increment**
  Besides the three parameters mentioned above, height increment should also be taken into consideration.

  In order to obtain a consistent laser spot size throughout multi-layer processes, a specific height increment must be applied with each successive layer. This increment determines the vertical shift of the process plane and directly affects layer alignment. Equation 2.4 derived by Zapara et al.[41] is used as a theoretical basis for calculating the optimal height increment for the multi-layer processes, where H_l represents the height increment per layer, with the cross-sectional area of the wire A_w, the bead width W_b and the speed ratio v_r.

$$H_l = \frac{A_w}{W_b} \cdot v_r \tag{2.4}$$

  As explained in the previous section, the laser spot size will be different when the focused point of the laser shifts to a higher or a lower position. Hence, with the higher wall built in the vertical deposition, the laser head. Therefore, the height increment serves as an important parameter in the thin-wall deposition stage of the experiments.

  When using a height increment smaller than the calculated value, it results in a measured part height greater than expected. In contrast, when a height increment larger than the calculated value is applied, it leads to a measured height lower than predicted. In both cases, the height increments used deviate from the theoretically calculated value; the deposition of consecutive layers would ultimately lead to a process failure due to the mismatch between the actual part height and the adjusted height of the process plane.

  If the theoretically calculated height increment is used, the final height of the produced part closely matches the intended process height, particularly at lower speed ratios. However, larger deviations occur at higher speed ratios, especially for aluminium alloys.

2.3 Challenges of Current Research

Despite the increasing maturity of LDED for various materials, the processing of aluminium alloys remains particularly challenging. Several issues have been repeatedly highlighted in the literature, and most of the persistent issues originate from the intrinsic material characteristics of aluminium and the strong sensitivity of the process conditions.

To begin with, a widely reported difficulty is the accumulation of heat during layer-by-layer deposition, which leads to building structural deviation and distortion. The strong dependence of temperature fields on the local process conditions means that small variations in the parameters can accumulate into large geometric changes over the build height. In addition, porosity formation presents a persistent challenge. Hydrogen-driven porosity is difficult to fully avoid and strongly dependent on melt pool dynamics and remelting behaviour across layers. Microstructure control is another focus in the literature, as the columnar-to-equiaxed balance, grain growth direction and solidification conditions directly influence mechanical performance.

These challenges highlight the need for experimentally grounded studies that examine how process parameters and build height influence geometry, microstructure and defect formation in wire-based LDED of aluminium. The research questions of this thesis are therefore formulated to address these gaps.

These limitations motivate a study that links process parameters, geometry development, microstructure, defects, and thermal behaviour in a unified framework.

Based on these gaps, the following research questions are formulated:

1. **How do key process parameters (laser power, travel speed, wire-feed rate) influence the geometry and microstructure of single-bead depositions?**
2. **How do process parameters and build height influence the as-built characteristics of multi-layer structures produced by wire-based LDED?**
3. **What material characteristics can be identified in the multi-layer aluminium deposits produced in this study?**

Chapter 3

Experimental Setups

3.1 Materials

The feedstock wire used in the experiments is the ER 5356 aluminium wires with a diameter of 1.0 mm. AA 2219 aluminium sheets were used as the substrates, cut to a dimension of 150 mm x 50 mm x 5 mm. Table 3.1 and 3.2 respectively show the composition of the wire feedstock and the substrate used.

Table 3.1: Composition of ER 5356 aluminium wires in wt%.

Material	Mg	Al	Cu	Fe	Si	Zn
ER 5356	4.5-5.5	Rem.	0.10	0.40	0.25	0.10

Table 3.2: Composition of AA 2219 aluminium sheets in wt%.

Material	Cu	Al	Mn	Fe	Zr	Zn
AA 2219	6.39	Rem.	0.29	0.11	0.13	0.04

In addition to the chemical composition provided by the supplier (Table 3.1 - 3.2), the microstructure of the 5356 feedstock wire was examined using optical microscopy(OM) and scanning electron microscopy(SEM). OM images taken showed a uniform matrix microstructure without visible segregation at lower magnifications, see Figure 3.1.

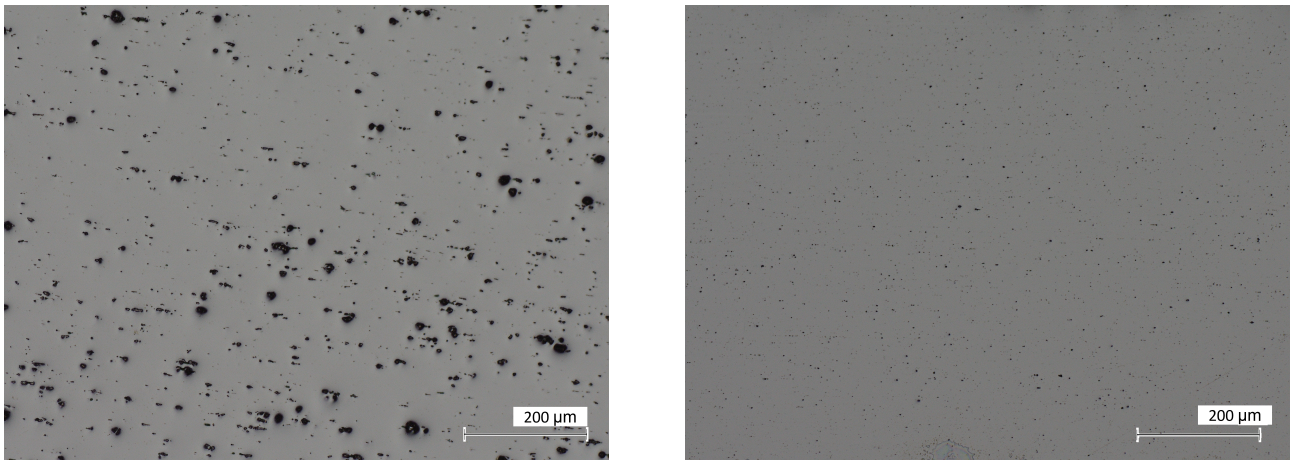

(a) OM image of the cross-section of the substrate

(b) OM image of the cross-section of the feedstock wire

Figure 3.1: OM image of the cross-sections of the substrate and the feedstock wire.

SEM observations at higher magnification revealed the presence of small, bright particles distributed within the matrix (Figure 3.2). To identify these features, energy-dispersive X-ray spectroscopy (EDS) analyses were conducted on both the matrix and the bright particles. The matrix composition was consistent, containing 5–6

wt.% Mg with the balance Al, and no detectable Fe. In contrast, the bright particles consistently exhibited a trace amount of Fe and Mn, together with slightly reduced Al and Mg contents. These inclusions are therefore considered intrinsic features of the feedstock wire.

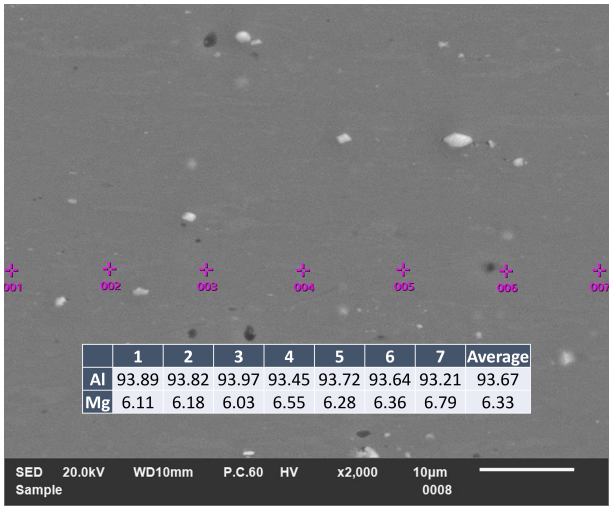

(a) SEM images and results of EDS analysis on the matrix of the feedstock wire

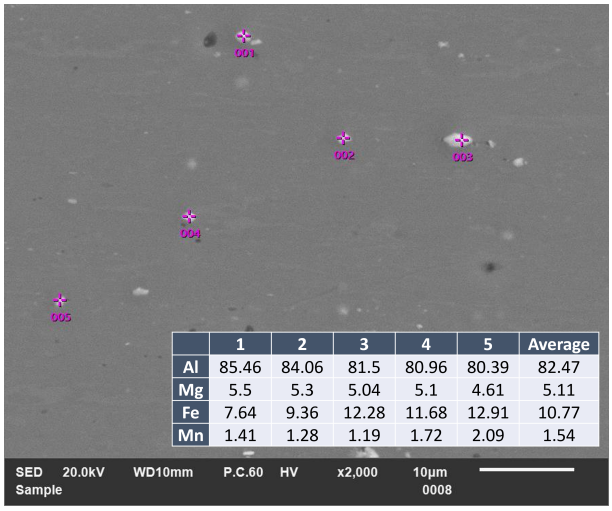

(b) SEM images and results of EDS analysis on the inclusion of the feedstock wire

Figure 3.2: SEM images and results of EDS analysis on the matrix and the inclusion of the feedstock wire.

3.2 Laser Equipment Set-ups

- **Laser System**
  The laser equipment used in the experiments is provided by the TU Delft. The laser consists of a Trudisk 8001 from Trumpf, which is a YAG laser with a maximum power of 8 kW attached to a CNC machine. Because of the highly reflective nature of aluminium alloys, it can cause severe damage to the laser head optics. To avoid the potential damage, the laser head is thus tilted by approximately a 5-degree angle away from the feed wire. In addition, the vapour released during processing may lead to blockage of the beam and accumulation on the lens, affecting the resultant energy density delivered to the workpiece. In order to deal with this issue, a compressed air cross jet is used to remove the fumes in front of the lens. Prior to deposition, the removal of oxide layers on the substrate surface is required, using a metal brush or grinding papers.

- **Wire-Feeding System**
  In the deposition experiments, a movable worktable and a wire-feeding system were used, aside from the laser system. The substrate was firmly clamped onto the worktable to ensure consistent positioning during deposition. The table was movable in linear motion along the horizontal axis, enabling a controlled path of the laser relative to the substrate and therefore defining the deposition direction.

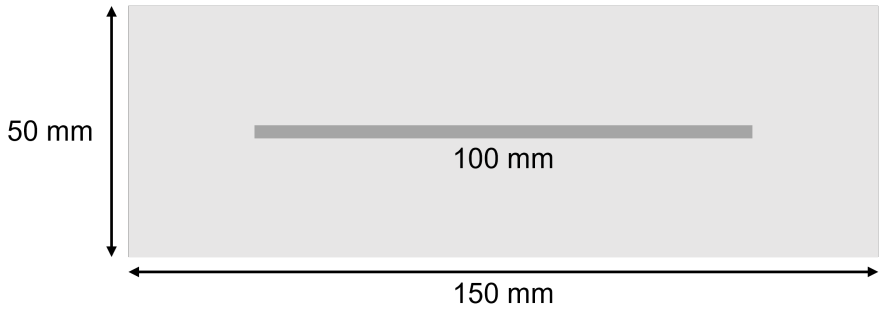

Figure 3.3: The schematic of substrate dimension and the positioning of the deposition.

The wire feedstock was added through a nozzle positioned at an inclination of approximately 30° to the substrate surface. The wire-feeding rate was controlled by a wire-feeder, which allowed the adjustment of the wire-feeding rate.

- **Coordination**
  For coordinate definition, the deposition direction was designated as the Y-axis (longitudinal), the perpendicular in-plane direction as the X-axis (transverse), and the build-up direction as the Z-axis (vertical). This coordinate system is used consistently throughout the subsequent analysis and discussions.

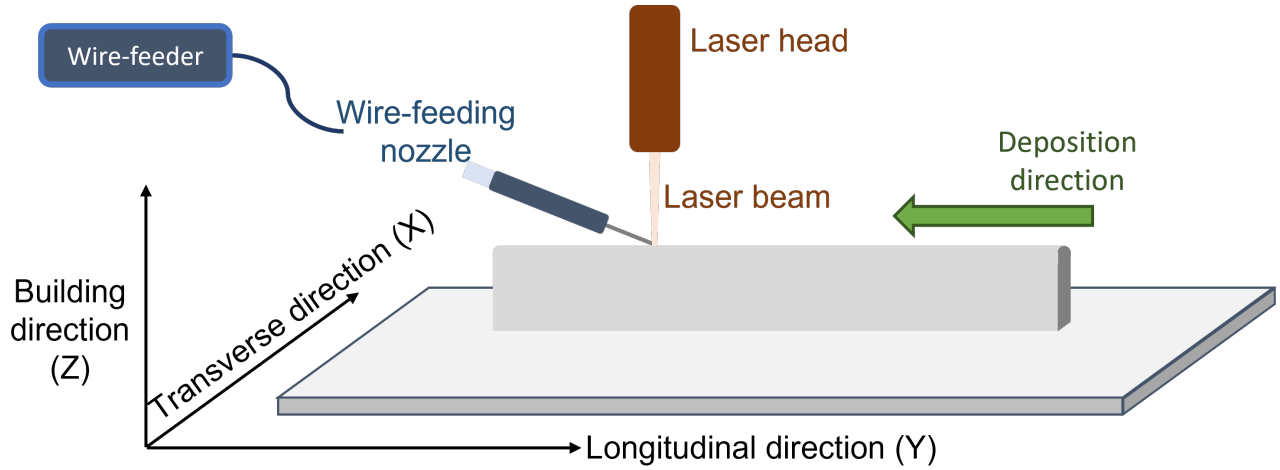

Figure 3.4: The schematic of the laser, substrate, wire-feeding setups and the definition of each direction of the samples.

3.3 Experimental Stages and Parameter Settings

The experiments were conducted in two major stages: **single-track depositions** and **multi-layer depositions**. This section summarises the parameter settings used for each sample in the two stages into tables.

3.3.1 Single-track Depositions

In the first stage, single-track depositions were expected to be made to investigate proper parameter levels and variation structures for each parameter. A range of proper parameters for stable depositions can then be established.

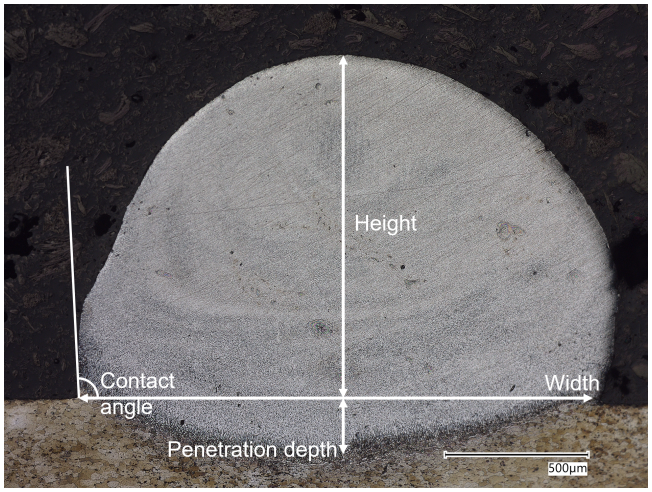

Figure 3.5: The definition of dimensional metrics for single-bead depositions.

Table 3.3: Process parameters used for single track depositions.

Sample	Laser Power (W)	Travel Speed (mm/s)	Wire-Feeding Rate (m/min)	Speed Ratio
ST1	2200	15	1.73	0.1153
ST2	2200	15	2.06	0.1373
ST3	2200	15	2.06	0.1627
ST4	2200	15	2.44	0.2067
ST5	2200	15	3.10	0.2380
ST6	2200	15	3.57	0.2753
ST7	2200	15	4.13	0.2833
ST8	2200	15	4.25	0.1785
ST9	2200	20	3.57	0.1428
ST10	2200	30	3.57	0.1190
ST11	2350	30	3.57	0.1190
ST12	2500	30	3.57	0.1190

3.3.2 Multi-layer Depositions

Once a stable process window was ensured, the experiments were continued to vertical deposition, and appropriate parameter settings for building thin-wall structures were also explored. The parameter settings used in this stage were selected from the stable and decent track from the previous stage.

In the multi-layer depositions, the laser power was gradually lowered over the first three layers, specifically 100W for each layer, to compensate for the initially colder substrate and to stabilise the melt pool once the temperature of the workpiece was elevated. This is a strategy in the process to improve bonding and reduce excessive heat and penetration in later layers.

With every three layers deposited, the laser head was lifted upwards by 2 mm to adjust to the wall in order to remain the focus distance and keep the positioning of the wire-feeder. Using the appropriate height increment is essential to ensure the consistency of the laser spot size and avoid insufficient melting during the deposition. The height increment of one thin-wall sample (TW6) was adjusted accordingly for each layer printed. The continuous adjustment of the Z-increment was made as a comparison, in order to evaluate the influence of different strategies on height increment on wall geometry and stability of the process.

Table 3.4: Process parameters used for multi-layer depositions. Laser power values indicate layer-dependent ramp-down (see Section 2.3.2). Δz indicates Z-increment strategy: per layer or every 3 layers.

Sample	Number of Layers	Speed Ratio	Laser Power (W)	Z-increment
TW1	6	0.238	2200→2100→2000	Δz every 3 layers
TW2	7	0.238	2200→2100→2000	Δz every 3 layers
TW3	12	0.238	2200→2100→2000	Δz every 3 layers
TW4	6	0.179	2200→2100→2000	Δz every 3 layers
TW5	12	0.179	2200→2100→2000	Δz every 3 layers
TW6	6	0.179	2200→2100→2000	Δz per layer

3.4 Geometrical and Distortion Measurement by 3D Scanning

The deposition geometry and substrate distortion of the deposited samples were analysed using an Artec Spider structured-light 3D scanner together with Artec Studio software. All samples across the single-tracks and thin-walls were scanned with an Artec 3D scanner from three directions before the resulting scans being fused to obtain a watertight mesh of each sample. Prior to every use of the 3D scanner, a standard calibration was conducted to the scanner to ensure the accuracy of the measurements and the alignment between the scanner and the software.

To facilitate precise measurements for dimensions and distortions, the 3D mesh and cross-sections were then exported to SolidWorks. The cross-sections exported to SolidWorks were presented as profiles, where measurement tools could be applied to obtain the geometry of the deposited tracks and walls (height, width and profile). Therefore, after the scans were completed, cross-sections were extracted at selected positions from different directions, in order to characterise both the deposition geometry and the substrate distortion.

Cross-sections were made from the 3D scans in three planes (XZ, YZ, and XY), as suggested in Figure 3.6. The choice of sectioning strategy was tailored to the type of information required:

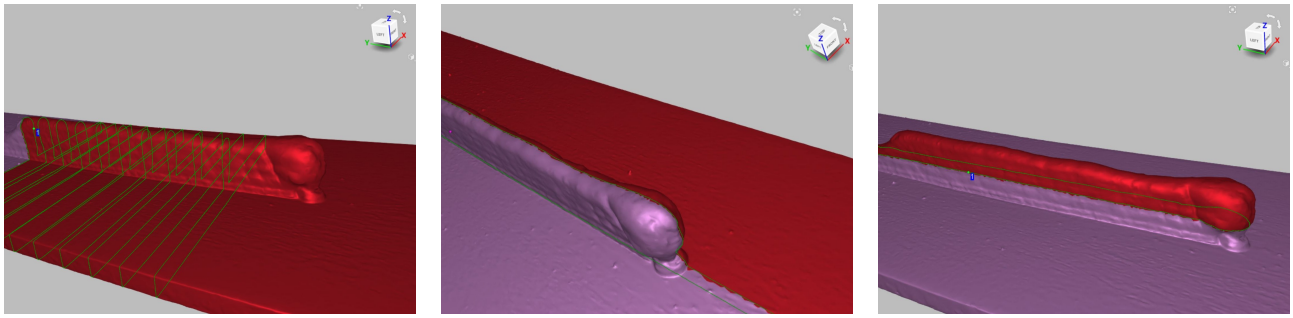

(a) Cross-sections of longitudinal direction (b) Cross-section of transverse direction (c) Cross-section of vertical direction

Figure 3.6: The scans in each direction and the cross-sections taken for measurements from each direction.

- **Y-direction (XZ plane/Longitudinal direction):**
  Along the deposition direction (Y-direction), the length of deposition was 100 mm. To capture possible variations in geometry and distortion along this length, ten cross-sections were taken in the XZ plane, each spaced evenly by 5 mm intervals. The cross-sections taken avoided the beginning and the end of the deposition for a more stable deposition shape. These sections allowed the deposition height and local distortion to be quantified at multiple positions, providing a representative average.

- **X-direction (YZ plane/Transverse direction):**
  In the transverse direction (X axis), the deposition was made centred on the substrate. Therefore, one cross-section was taken at the mid-X position (YZ plane). Considering the deposition width, the section taken right in the middle is considered sufficient to capture and represent the substrate distortion in the transverse direction.

- **Z-direction (XY plane/vertical direction):**
  In the vertical direction (Z axis), one cross-section was taken at the mid-height of the deposited wall (XY plane), avoiding the proximity to the substrate and the top of the wall. Although only a single plane was extracted, its intersection with the ten longitudinal sections (XZ plane) provided ten points for wall width. Hence, the XY cross-section was sufficient for quantifying width variations without requiring additional vertical slices.

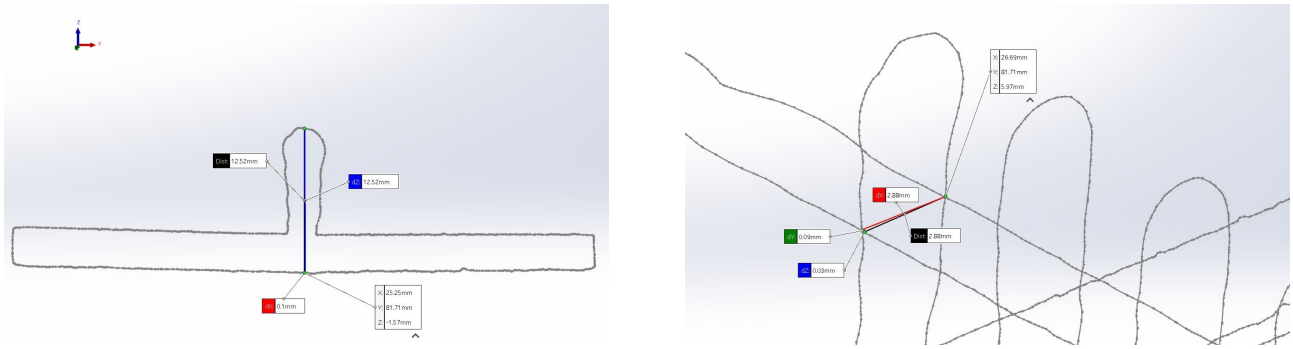

Figure 3.7: The demonstration of the distance measuring in SolidWorks for the height and the width of thin-wall samples.

In summary, ten sections along the deposition length (XZ plane) captured both geometry and distortion trends, while one transverse (YZ) and one vertical (XY) section provided representative information in the other two orthogonal directions.

This combined workflow allowed both qualitative visualisation (cross-sectional profiles, deviation maps) and quantitative measurements (dimensional values, distortion statistics) to be obtained. The methodology is summarised in Figure , showing the scanning process, cross-section generation, and CAD-based measurement.

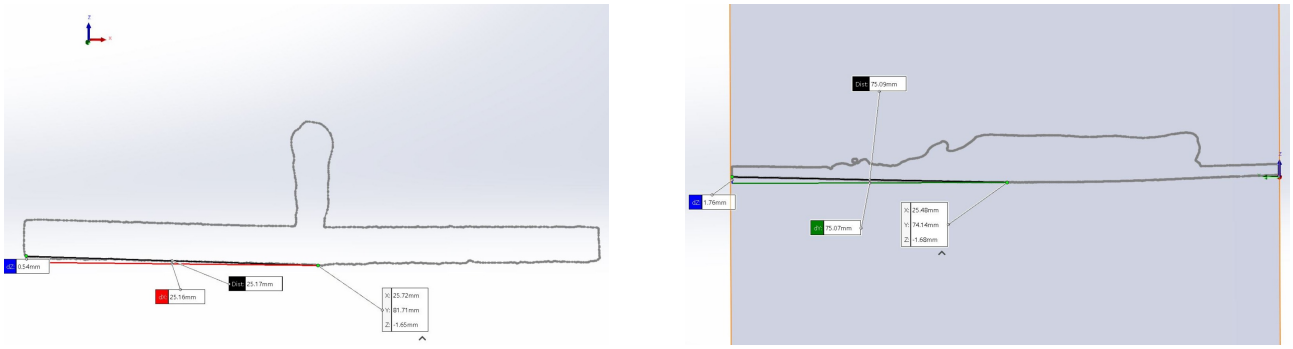

Figure 3.8: The demonstration of the distance measuring in SolidWorks for distortion for the XZ direction and the YZ cross-sections.

- **Dimension Measurements**
  Dimensional features such as width and height (for both single-tracks and thin-walls) were measured from the 3D-scanned profiles. For thin-wall samples, the overall wall height and mid-height width were extracted from the longitudinal profiles and averaged over ten equally spaced points along the wall. The average layer thickness was derived by dividing the total wall height by the number of deposited layers, representing the mean layer build-up per deposition cycle.

- **Distortion Measurements**
  Mid-span deflection δ was defined as the vertical displacement between the midpoint and the edge of a substrate cross-section. The deflection was measured in ten cross-sections taken along the deposition length, and the average value δ was reported.

  In this work, the size of the substrates was all identical. However, to allow comparison across other cases of different sizes and to generalise the results, the deflection was normalised by the half-span length $L/2$, yielding a dimensionless distortion metric δ^* according to Equation 3.1.

  Normalised deflection measurement was computed as

$$\delta^* = \frac{\delta}{L/2} \tag{3.1}$$

  where $L/2$ is the half-span (distance from centre to the substrate edge) in the corresponding direction.

3.5 Characterisation and Porosity Analysis

3.5.1 Sample Preparation

To investigate the microstructure of the samples, standard metallographic preparation was carried out. The cross-sections of the deposition samples of single-track and multi-layer were prepared for microstructure investigation. The specimens were first cut into a slim strip, taking a small section in the middle part of the deposition to avoid unstable parts at the beginning and the end of the deposition. Then, they were subjected to cold mounting using a conductive resin. In order to prevent thermal or mechanical damage, cold mounting was chosen over hot mounting. The conductive resin also ensured compatibility with subsequent scanning electron microscopy (SEM) analysis.

After curing of the resin, the mounted samples were subjected to grinding and polishing to produce a flat and reflective surface. Starting with a series of grinding processes using silicon carbide (SiC) papers (from 180 to 2400 grit size) with running water, followed by polishing with diamond suspensions down to a submicron scale to remove surface deformation and reveal the true microstructure. First, a 3 μm diamond suspension was used to remove the scratches left from prior grinding, and in the second step, 1 μm diamond suspension was used to obtain a mirror-like surface finish.

Etching was then applied using a suitable chemical reagent specific to the alloy system, in order to enhance the contrast between different microstructural features such as grain boundaries, phases, or inclusions.

To reveal the microstructure, 2% nital solution was used to etch the specimen surface for approximately 10 s, followed by a thorough wash with isopropanol and subsequent drying using an air blower.

3.5.2 Optical Microscope

The polished and etched surfaces were examined by optical microscopy to capture general microstructural features and to perform an initial qualitative assessment.

The etched specimens were analysed using the Keyence VHX-7000N Digital Microscope. It is a reflected light microscope which can be used to observe metallic surfaces. The illuminating system of the microscope generates visible light, which is used for metallographic observations. A Kohler system directs the generated light beam from the illuminating system towards the specimen being observed, and using the same system, the reflected light rays from the surface of the specimen are used to form an image of the specimen surface [70]. The relative ease of operation of optical microscopes justifies their extensive use for microstructural characterisation; however, the limited resolution at high magnifications is a drawback of these microscopes.

3.5.3 Scanning Electron Microscope

For higher magnification and more detailed surface analysis, scanning electron microscopy (SEM) was employed. SEM is a technique which enables us to achieve resolutions, providing insights into surface morphology, phase distribution, and, when applicable, elemental composition through energy-dispersive X-ray spectroscopy (EDS). This combined approach allowed for a comprehensive characterisation of the microstructure, aiding in the interpretation of processing effects and material performance. The SEM equipment used in this work was the JEOL JSM-IT100.

The resolution of a microscope is limited by the wavelength of the incident beam. In optical microscopy, the incident beam is constituted of packets of photons whose wavelength is limited to 400 nm. In the case of matter waves, the De-Broglie wavelength is dependent on the momentum of the wave, which is in turn controlled by the acceleration voltages. By using electron beams, much lower De-Broglie wavelengths are achievable, depending upon the acceleration voltages, thereby achieving much higher resolutions. Conventional SEM have a typical energy range of (1-30 keV). The incident/primary beam of electrons interacts with the constituents of the sample and emits secondary electrons, which are detected by a Everhart-Thornley detector. The beam is raster scanned over the entire sample surface, thereby generating an image of the entire surface. A backscattered electron detector is also used in some cases. The backscattered electrons originate from the subsurface regions of the sample, and their intensity/contrast is directly dependent on the atomic number of the constituent element. These electrons therefore helps us to gain a better understanding of the subsurface regime of the sample and also provide a quasi-elemental mapping of the surface.

3.5.4 Electron Backscatter Diffraction (EBSD)

Conducting electron backscatter diffraction (EBSD) analysis can help obtain deeper and further insights into crystallographic structure and grain orientation on selected polished samples, facilitating the understanding of the relations between the grain morphology, microstructure and properties.

Prior to EBSD scanning, the samples went through further preparation steps to ensure adequate pattern quality, processed differently from the preparation steps for optical microscopy. The samples required polishing with a mixture of colloidal silica (OP-S), with a longer polishing time than diamond suspension.

EBSD measurements were carried out using a ThermoFisher Scientific Helios G4 PFIB Uxe scanning electron microscope equipped with an AMETEK EDAX EBSD detector. All scans were performed at an acceleration voltage of 15 kV and a beam current of 13 nA. A step size of 0.65 μm was used during the scans. EBSD data were acquired in mapping mode, and the resulting datasets were post-processed using EDAX OIM Analysis v.8.

Hence, the image quality (IQ) maps and corresponding inverse pole figure (IPF) orientation maps are generated as results. Grain boundary overlays and grain-size estimations were also extracted as needed. All EBSD maps reported in this study represent the as-built microstructure without additional thermal treatment.

For each selected thin-wall specimen, EBSD scans were acquired from selected regions to capture the variation in microstructure along the build height. Specifically, a "TOP" region near the free surface and a "BOT" region near the fusion line were examined. These locations were chosen to highlight microstructural differences associated with changes in thermal gradients and cooling conditions during the DED process.

3.5.5 XRD Analysis

X-ray diffraction (XRD) was performed to identify the crystalline phases present in the deposition. The measurements were carried out using a Bruker D8 Discover diffractometer and Eiger-2 500k 2D-detector, equipped with a Cu α radiation source (λ = 1.5406 A). The scan was performed over a continuous 2θ range of 10-150 ° with a step size of 0.02 °.

The XRD patterns were compared with reference data from the Crystallography Open Database (COD) and International Centre for Diffraction Data (ICDD) to identify the corresponding phases based on the calculated interplanar spacing (d-spacing) obtained using Bragg's law:

where n is the diffraction order (taken as 1), λ the X-ray wavelength, d the interplanar spacing, and θ the Bragg angle.

The analysis was aimed at detecting possible formation of intermetallic compounds (e.g., Al_3Mg_2 or beta-phase) that have been reported in previous studies of Al 5356 alloys processed by laser and arc-based additive manufacturing methods.

3.5.6 Porosity Analysis

Porosity analysis was conducted using the image processing software *ImageJ*, see Figure 3.9. The images of the samples collected from optical microscopy were first imported. The colour threshold was applied to the images and adjusted to cover and capture the porous area in the deposited parts. Afterwards, based on the selected region, the measurement could be made.

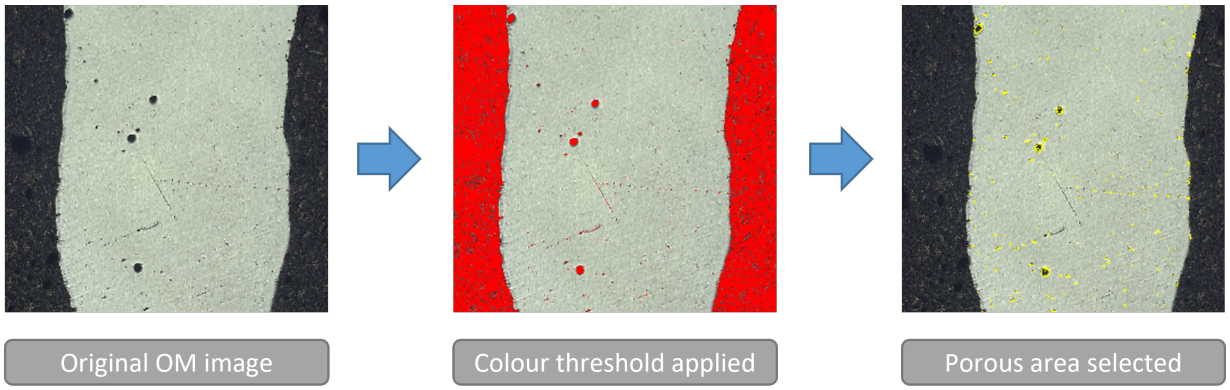

Figure 3.9: The process of porosity analysis in ImageJ

3.6 Thermal Analysis

Thermocouples can be used to obtain the temperature gradient during the thermal cycles based on the thermoelectric effect. The two wires of a thermocouple are respectively attached to a reference point and a measuring point, and then a current is established, detected by a voltage. This voltage is proportional to the temperature difference between the junction and the reference point, allowing reconstruction of the junction temperature using standard calibration tables. Thermocouples offer proper response when the junction is small, making them suitable for transient thermal monitoring during the deposition process.

The data obtained in the experiments were recorded by K-type thermocouples. Two K-type thermocouples were attached to the substrate by resistance spot welding, positioned at the mid-length of the deposited thin-wall, 10 mm and 20 mm, respectively, from the edge of the substrate, see Figure 3.10. This setup allowed measurement of the thermal response during laser processing without disturbing the melt pool.

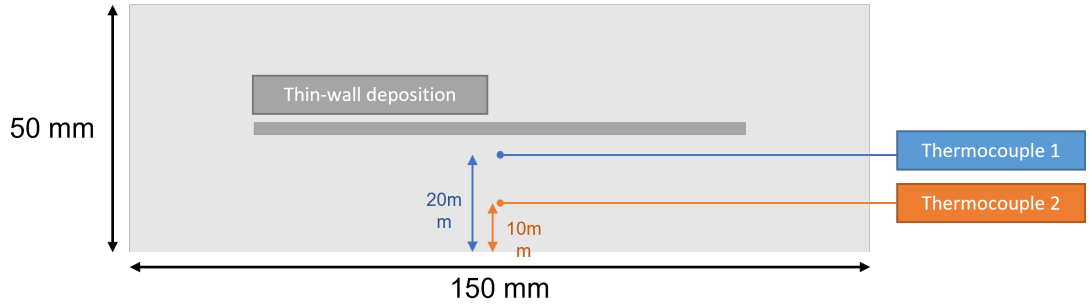

Figure 3.10: Schematics of positioning of thermocouples in thermal analysis

The thermocouple was connected to a data acquisition system to record the transient temperature changes throughout the deposition process. The temperature-time data were recorded using a Yokogawa DL716 digital oscilloscope. The effective sampling interval was at 5 ms, corresponding to a sampling rate of 200 Hz. This temporal resolution was sufficient to capture the thermal cycles associated with each deposited layer, while maintaining a manageable data size for analysis.

This test aims to monitor the thermal history during thin-wall deposition using a thermocouple. Recording the temperature profile provides information about the heating cycles and cooling rates during the vertical building, which in turn influence melt pool stability, the connection between layers, and the resulting microstructure.

The obtained data indicate that while printing multiple layers, the base material cools down to room temperature in approximately 60s - 120s. This waiting time in between each layer is needed in this setup in order to reposition the work table to the starting point for the next deposition.

Since the time interval between subsequent layer depositions was not strictly controlled due to table repositioning, the variation results in a slightly different pre-heat condition for each deposition.

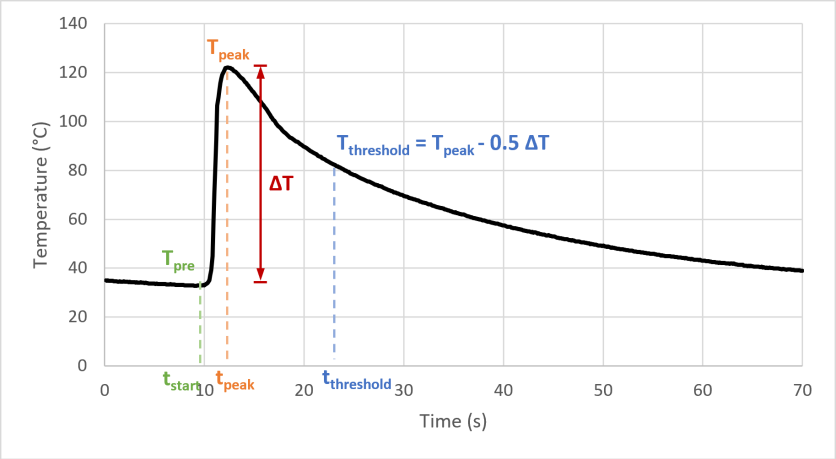

Figure 3.11: Definition of the peak temperature, the preheated temperature, the heating temperature, and the cooling threshold temperature in thermal analysis.

Figure 3.11 gives the demonstration of how the thermal parameters are defined in a cycle, and the parameters used in the calculation is defined as below:
The start of heating, t_{start}, was defined as the moment when the temperature began to rise consistently above the baseline. The heating onset was detected by the derivative of the smoothed temperature signal (dT/dt). The heating start time $t_{start}$was defined as the first time where dT/dt exceeded 5 °C/s for at least 0.2 s. The pre-heat temperature T_{pre} was taken as the temperature 0.5 s before t_{start}. The peak temperature T_{peak} corresponded to the maximum value reached in each cycle. A threshold temperature $T_{threshold}$, was introduced as the temperature cooling down to 50% of the peak rise δT (T_{peak} - T_{pre}) after reaching the T_{peak}. Similar relative thresholds have been used in thermal-cycle characterisation to provide a consistent reference level for evaluating cooling rates. The 50% point avoids noise near the lower range and reduces sensitivity to minor fluctuations in the temperature plateau.

With the times and temperatures defined, the heating rates and cooling rates were then calculated as:

$$\dot{T}_{\text{heat}} = \frac{T_{\text{peak}} - T_{\text{pre}}}{t_{\text{peak}} - t_{\text{start}}}$$

and

$$\dot{T}_{\text{cool}} = \frac{T_{\text{peak}} - T_{\text{thershold}}}{t_{\text{threshold}} - t_{\text{peak}}}$$

.

3.7 Hardness Test

The hardness testing was carried out to determine the hardness of the deposited part of 5356 aluminium alloy. The hardness was measured at multiple points along the height of the cross-section of thin-wall samples to determine the vertical variation of hardness along the building direction, as shown in Figure 3.12. Vickers hardness measurements were taken using a diamond indenter of HV 0.2, and a 10x objective lens was used

for indentation imaging. A total of 21 indentation points were taken at intervals of 0.5 mm, starting from the substrate.

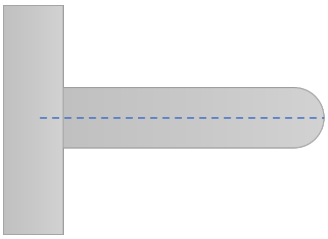

Figure 3.12: Schematic of hardness measurement indentations taken for thin-wall depositions

Chapter 4

Results

This chapter presents the experimental results obtained from two stages of experiments: **single-bead depositions** and **multi-layer depositions**. The main focus is to describe the effects of process parameters on the resulting geometries, porosity, and distortion. The results are supported by OM and SEM observations, measurements for dimensions and distortions, thermal analysis and EBSD analysis. The findings presented here provide the basis for the discussion in Chapter 5, where the correlations between process parameters and observed characteristics are further analysed.

4.1 Single-Bead Depositions

4.1.1 Bead Geometries and Dimensions

In the single bead deposition stage, three primary parameters were systematically varied: **laser power, travel speed, and wire-feeding rate**. The parameter variation was shown in Table 3.3. The objective of this stage was to establish how each parameter individually influences the resulting bead geometry, specifically bead **width** and **height**, and to identify conditions that lead to stable versus unstable depositions.

Bead dimensions were measured and compared across parameter sets, as defined in Section 3.4, enabling quantification of trends such as increasing width with higher power or decreasing height with higher travel speed. The ratio of bead height to width (aspect ratio) was also considered as a measure of deposition stability and suitability for multi-layer building.

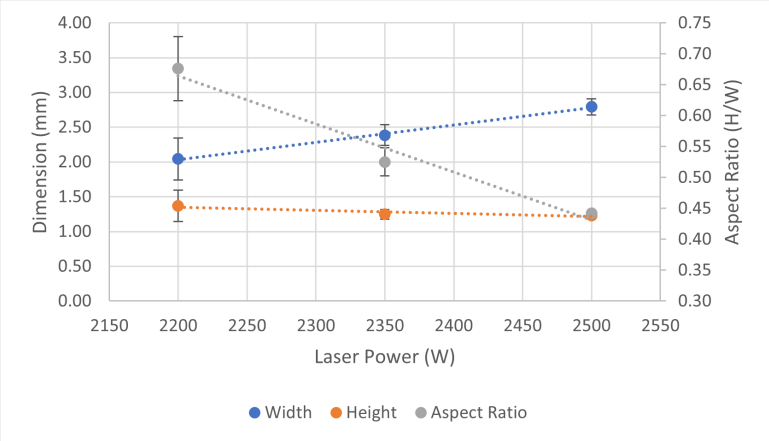

Figure 4.1: Dimensional metrics developing trend with increasing laser powers (with fixed travel speed = 30 mm/s and wire-feeding rate = 3.57 m/min).

Figures 4.1 - 4.3 summarises the effect of laser power, travel speed and wire-feeding rate on bead geometry (width, height, and aspect ratio). In all cases, increasing the parameter value resulted in systemic changes of dimensional metrics.

Figure 4.1 shows the dependence of the bead geometry on laser power. The bead width increases from 2.04 mm to 2.79 mm, showing a clear increasing trend, while the bead height goes down from 1.37 mm to 1.23 mm,

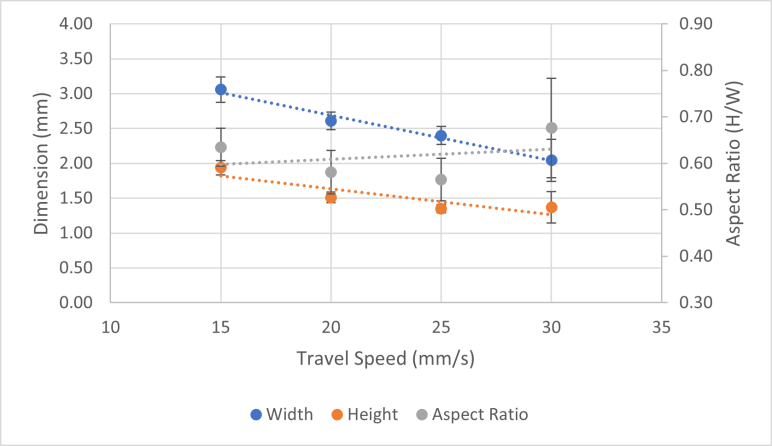

Figure 4.2: Dimensional metrics developing trend with increasing travel speeds (with fixed laser power = 2200 W and wire-feeding rate = 3.57 m/min).

with a slight decreasing trend. As a result, the aspect ratio showed a drastic decline accordingly, from 0.68 to 0.44.

For travel speed, in Figure 4.2, both the bead width and the bead height lowered with increasing speed. The bead width decreases from 3.06 mm to 2.04 mm, while the bead height decreases from 1.94 mm to 1.37 mm. Based on the fitted trendline, the aspect ratio shows an increasing tendency with travel speed. However, this result is strongly influenced by the data point at 30 mm/s. At a travel speed of 30 mm/s, the bead width and height both show small deviations from the fitted trend. While the bead width stays close to the regression line, the bead height appears slightly higher than expected. Consequently, the aspect ratio at this condition deviates more drastically from the otherwise consistent decreasing pattern observed at lower speeds.

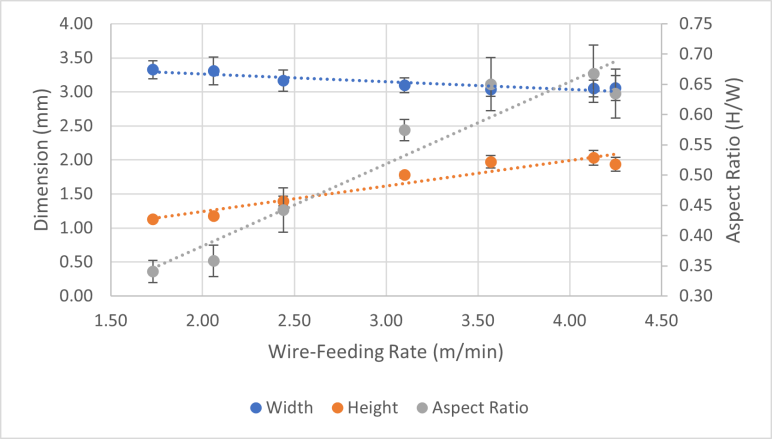

Figure 4.3: Dimensional metrics developing trend with increasing Wire-Feeding Rates (with fixed laser power = 2200 W and travel speed = 30 mm/s).

For wire-feeding rate (Figure 4.3), although individual data points fluctuate slightly, the overall tendency is captured by the trend line, and an opposite trend to the increasing laser power was observed. An increasing wire-feeding rate caused the bead width to decrease from 3.33 mm to 3.04 mm, and the bead height to increase from 1.13 mm to 2.03 mm. Collectively, they resulted in a strong increasing trend in the aspect ratio, from 0.34 to 0.67.

In addition to the geometric metrics of the deposited beads, the penetration depth and the contact angle were measured to evaluate the interaction between the feedstock material, the molten pool and the substrate. The penetration depth reflects how far the molten metal penetrates into the substrate. To complement the penetration depth, the contact angle was also measured as an indicator of wetting behaviour, showing how well the material wets and spreads onto the surface. Other than the surface tension, processing conditions also have a certain effect on the wetting behaviour in the deposition. Together, these two parameters provide complementary information about melt–substrate interaction.

Figure 4.4 - 4.6 summarises the effect of laser power, travel speed and wire-feeding rate on how single-bead

depositions bond with the substrate (penetration depth and contact angle). Elevating each parameter value resulted in systemic changes in the metrics.

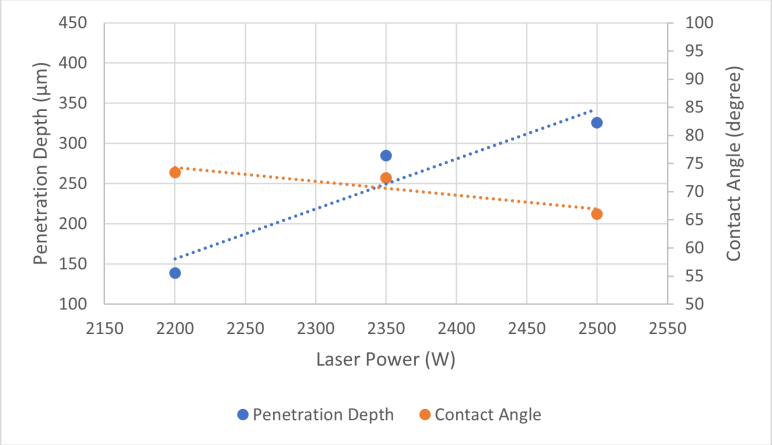

Figure 4.4: Contact angle and penetration depth developing trend with increasing laser powers (with fixed travel speed = 20 mm/s and wire-feeding rate = 3.57 m/min).

In Figure 4.4, with increasing laser power, the penetration depth showed a clear increasing trend, going up from 145 μm to 320 μm. Meanwhile, the changes in contact angle exhibit a rather slight decrease, from 74 ° to 64 °.

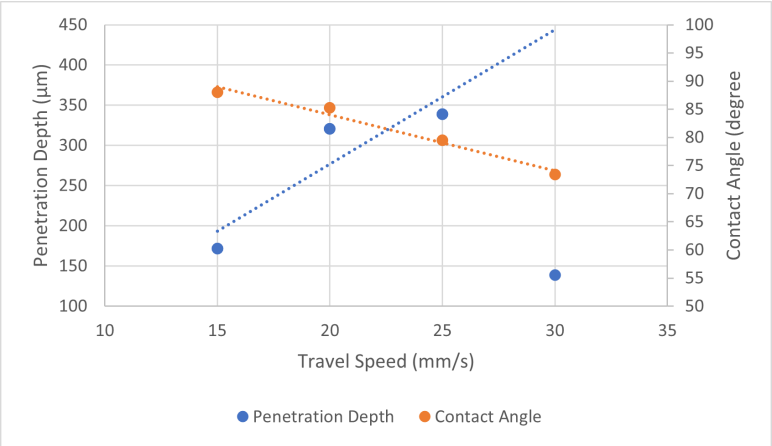

Figure 4.5: Contact angle and penetration depth developing trend with increasing travel speeds (with fixed laser power = 2200 W and wire-feeding rate = 3.57 m/min).

Figure 4.5 shows the effect of travel speed on the contact angle and penetration depth, the data points fluctuated rather greatly. The contact angle exhibited a clear, consistent decrease with increasing travel speed. For penetration depth, the values increased steadily between 10 and 25 mm/s, whereas the data point at 30 mm/s deviated significantly from this trend, showing a considerably lower value. The fitted trendline was drawn based on the data from 10 to 25 mm/s to reflect the general increasing tendency, while the 30 mm/s point is included for completeness.

Figure 4.6 shows the relation of the contact angle and penetration depth with wire-feeding rate. The penetration depth drops from 425 μm to 175 μm, exhibiting a clear decreasing trend, while the contact angle goes up from 60 ° to 86 °.

Deposition stability was assessed through both visual inspection and dimensional consistency. Stable beads were defined as continuous tracks with smooth edges, uniform wetting, and minimal spatter. Unstable conditions included balling, humping, lack of fusion, or irregularities along the bead.

The outcome of this stage is a preliminary process window, defining the operational ranges of power, speed, and feed rate that yield stable single beads. These findings provide the foundation for subsequent multi-layer deposition trials, where layer stacking and cumulative effects such as distortion become significant.

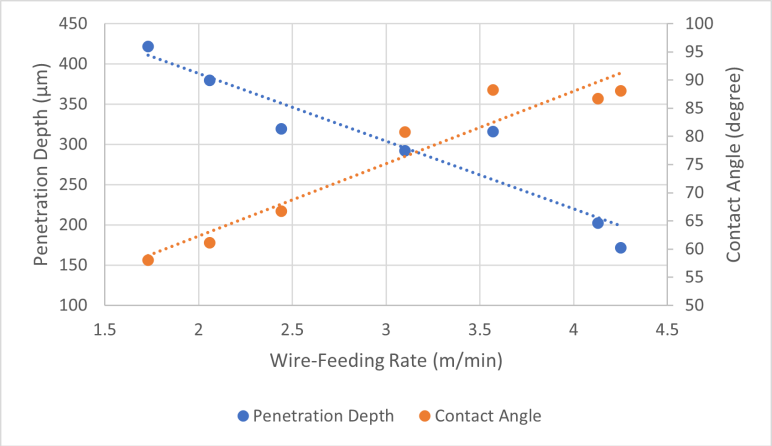

Figure 4.6: Contact angle and penetration depth developing trend with increasing wire-feeding rates (with fixed laser power = 2200 W and travel speed = 20 mm/s).

4.1.2 Microstructures

Other than bead geometries and their changes regarding each distinct process parameter, the etched cross-sections of the single-bead depositions were taken to capture the detailed microstructure of the deposition.

In the optical microscopy images of etched single-bead samples, they exhibit irregular patterns across the bead surface, characterised by darker and lighter regions alternating, see Figure 4.7. The four selected samples all have different heat inputs and feeding rates. Comparing the four samples, it can be concluded that there is no specific pattern or alignment for where the darker and the lighter regions are distributed.

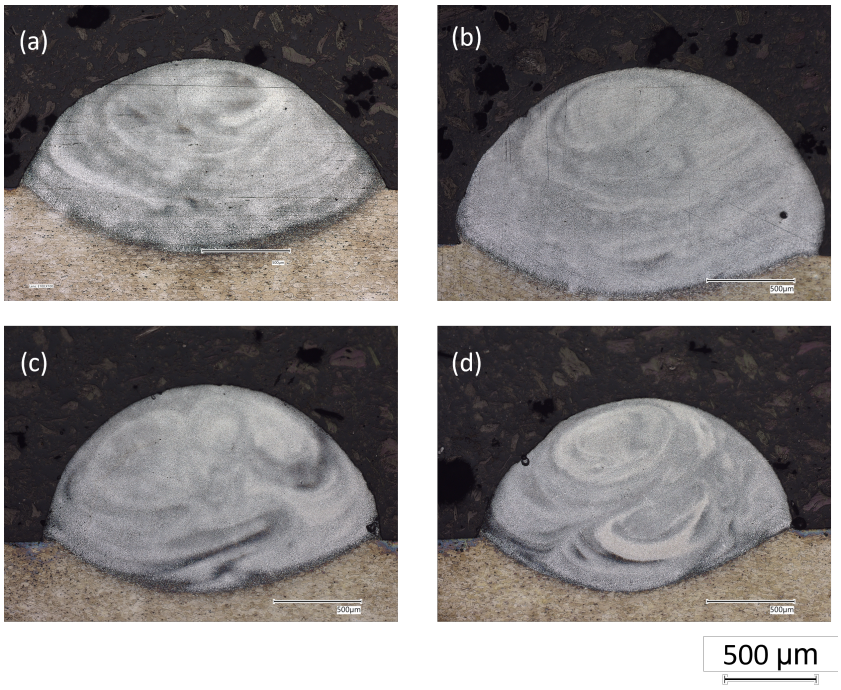

Figure 4.7: Representative etched cross-sections from selected single-bead depositions. (a) ST 2; (b) ST 4; (c) ST 8; (d) ST 9.

Enlarged micrographs were taken at higher magnifications, see Figure 4.8. In the darker region, the grains appear linear and more closely packed. Meanwhile, in the lighter region, no specific direction of grains is observed, and the grains are finer. The contrasts of alternating colours appeared to correspond to variations in grain arrangement.

To investigate the potential compositional variation associated with these contrast differences, EDS measurements were performed along a horizontal line across an enlarged region. Measurements were conducted under

two magnifications (×300 and ×500), and a total of five EDS point analyses were acquired at each magnification, see Figure 4.9.

The EDS results showed that the darker regions exhibited compositions consistent with the nominal feedstock wire (see Section 3.1), particularly in Mg and Al content. In contrast, the lighter regions displayed a detectable amount of Cu, with a slight reduction in measured Mg. The detected Cu comes from the substrate alloying element (see Section 3.1 for the composition of the substrate). Several individual data points were excluded from analysis due to unexpected carbon content, which was attributed to surface contamination or local artefacts from sample preparation rather than actual alloy composition.

Overall, the compositional differences observed between lighter and darker regions were small but consistent across magnifications.

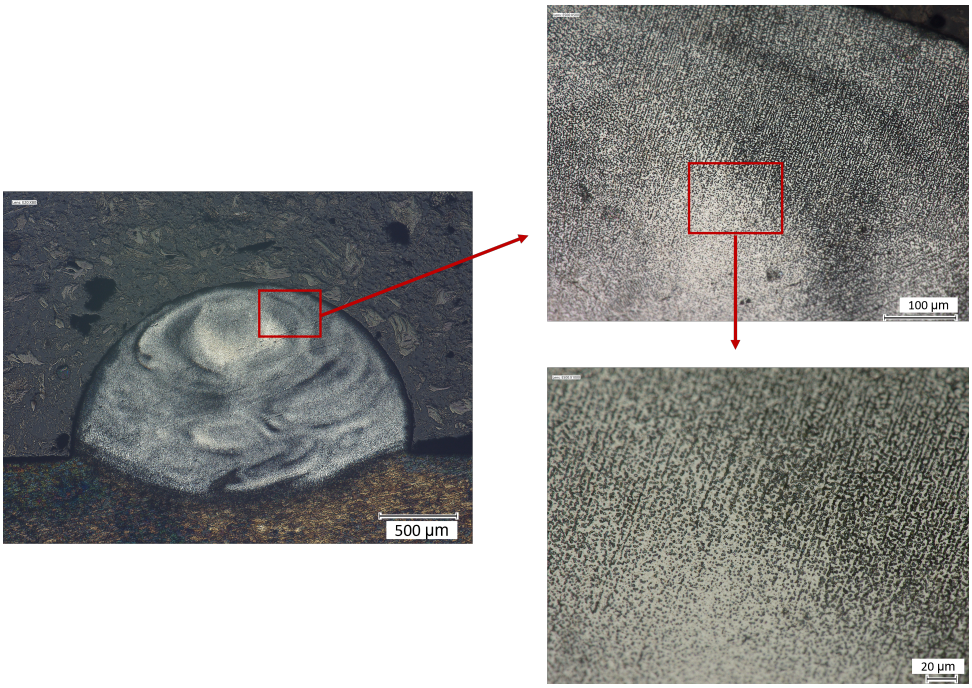

Figure 4.8: Representative etched cross-section from single-bead deposition and highlighted regions.

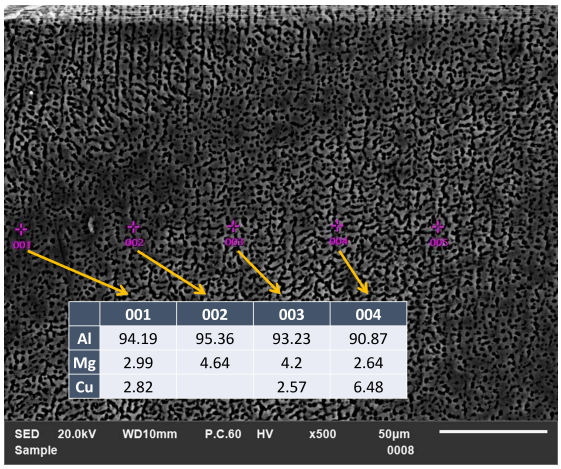

(a) Magnification: x300

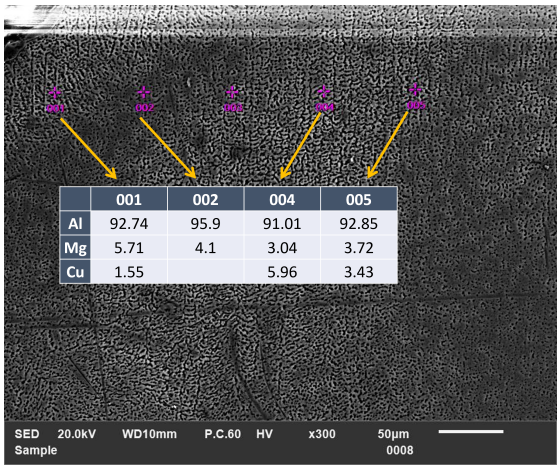

(b) Magnification: x500

Figure 4.9: The EDS point measurements for the enlarged region of the cross-section of etched single-bead deposition.

4.2 Multi-Layer Depositions

Following the single-bead investigation, multi-layer depositions were performed to evaluate how repetitive stacking affects the overall resultant quality. This section presents the evolution of shape, dimensions, porosity formation, and substrate distortion. The aim is to understand the cumulative effects of the process parameters on the structural integrity and stability of the deposited walls. The parameter sets used for multi-layer depositions were shown in Table 3.4.

4.2.1 Shape Evolution and Dimensional Analysis

- **Thin-wall Shape**
  All thin-wall samples produced under the tested parameter sets appeared stable and consistent in shape to the naked eye. Inevitable irregularities were observed at the initiation and termination points of each wall (see Figure 4.10), which were due to a manual operation issue on syncing the movement of the laser and the wire-feeder. The middle sections, in contrast, were more stable and representative of steady-state deposition.

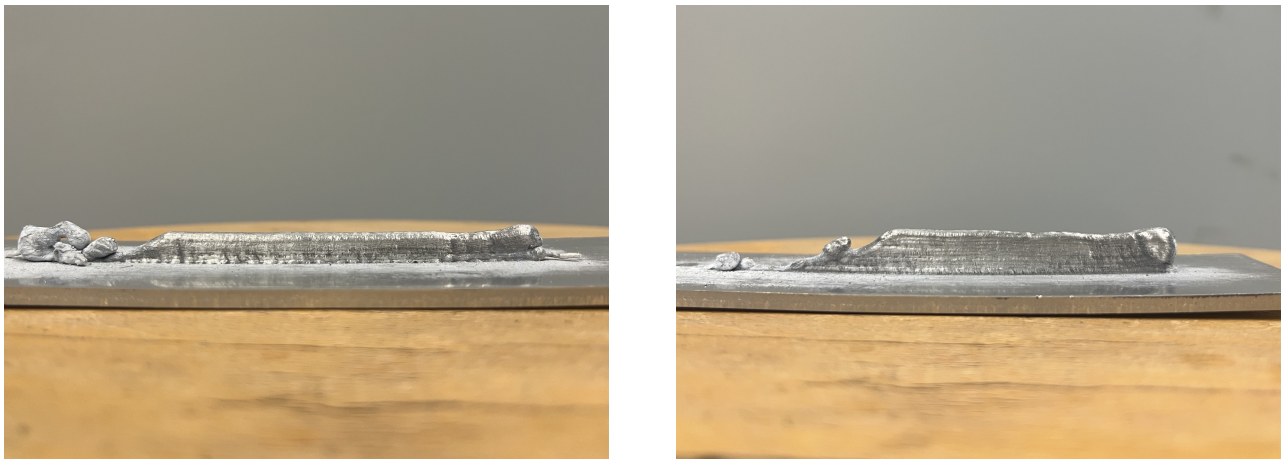

Figure 4.10: The side views of selected thin-wall samples (6-layer and 12-layer).

In addition to the irregularities in the longitudinal direction, a difference in wall width was also observed in the building direction of the thin-walls. In all thin-wall samples, the first deposited layer appeared narrower than the subsequent layers. This feature was consistently observed in the cross-section images (Figure 4.11). The layer width increased noticeably from the first to the second layer, after which it remained relatively constant throughout the build height.

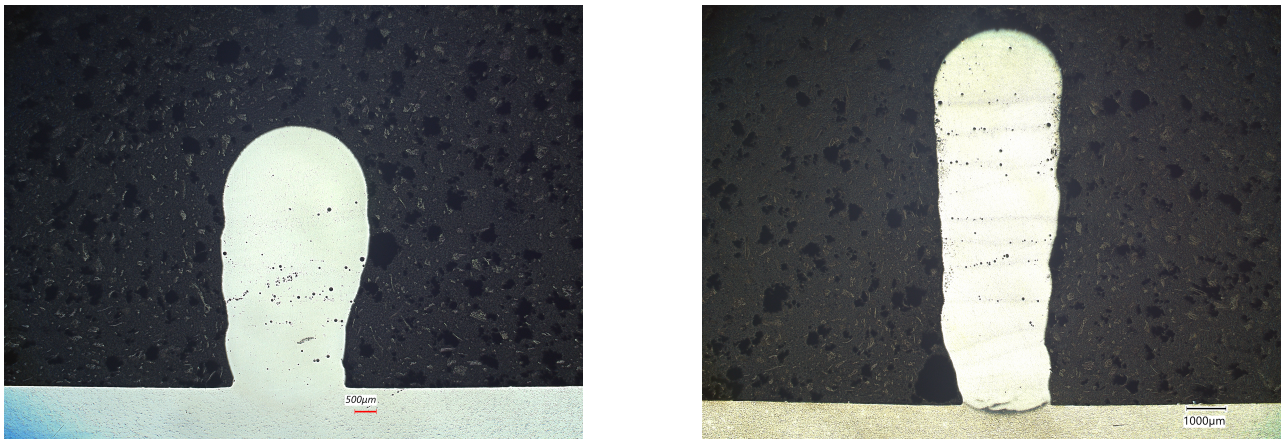

Figure 4.11: The side views of selected thin-wall samples (6-layer and 12-layer).

- **Thin-wall Dimensions**
  The dimensional measurements of the multi-layer thin walls were performed to evaluate the consistency

of layer stacking and to verify whether the geometric trends observed in single-bead depositions persisted in the multi-layer condition. Dimensional measurements (wall width, height, average layer height) for the multi-layer depositions are summarised in Table 4.1.

The overall wall height increased with the number of deposited layers and was higher at a travel speed of 20 mm/s compared to 15 mm/s (Table 4.1). Conversely, the wall width was slightly larger at 15 mm/s, although the difference between the two travel speeds was less pronounced than in overall height. The average layer thickness, derived from the ratio of total deposition to the number of deposited layers, was approximately 0.62 mm to 0.76 mm. It followed a similar trend to the overall wall height, showing only a slightly higher value with higher travel speed.

Table 4.1: The dimensional measurements (wall height, width, average layer height) for thin-wall depositions.

Sample	Number of Layers	Width (mm)	Height (mm)	Average Layer Height (mm)
TW1	6	3.06	4.26	0.71
TW2	7	2.87	4.72	0.67
TW3	12	3.11	9.16	0.76
TW4	6	3.31	3.75	0.63
TW5	12	3.67	7.46	0.62
TW6	6	3.46	3.97	0.66

4.2.2 Microstructural Analysis

- **OM Results**
  Aside from physical shape and dimensional analysis, internal microstructure also has a significant influence on the resultant properties of the depositions. An etched cross-section of a 6-layer thin-wall sample was selected, and a series of optical microscopy images was taken under different magnifications. The images reveal clear variations in microstructural morphology along the height of the thin wall. These differences are evident both at the scale of the entire wall and within individual deposited layers.

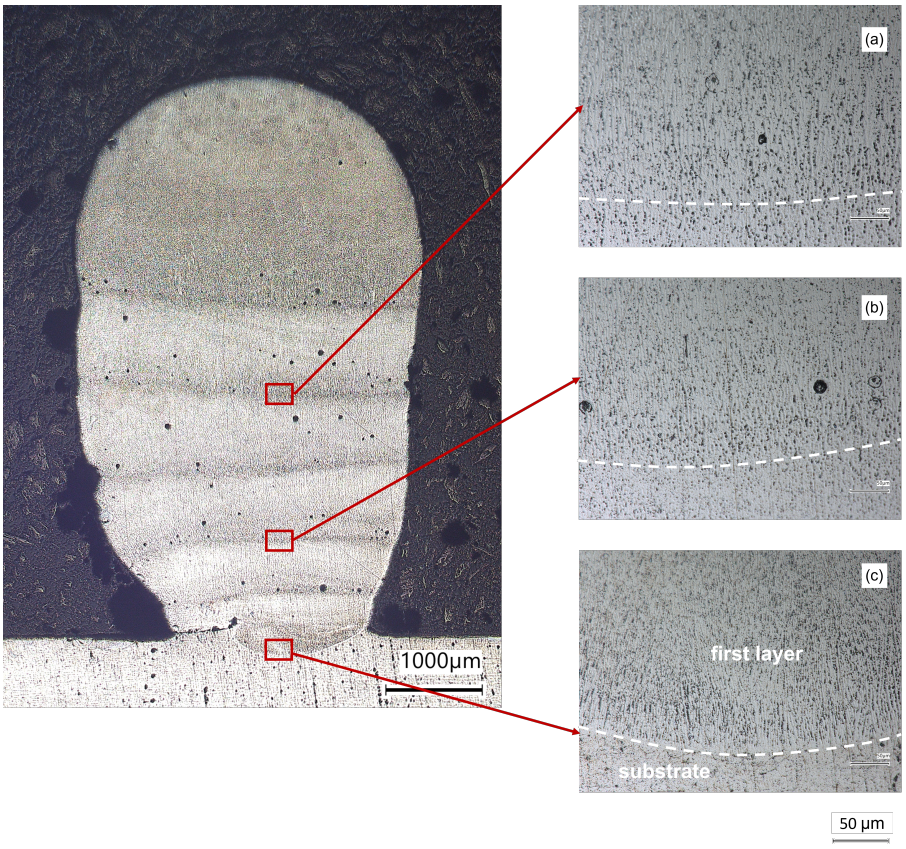

Figure 4.12: Micrographs of selected positions from a 6-layer thin-wall deposition. (The dotted lines mark the transitions between layers.)

Figure 4.12 shows representative micrographs of a thin-wall deposition at 3 positions along the building directions, as indicated with red boxes. The micrographs taken from the middle part of the multi-layer deposition exhibit similar microstructural features; thus, only two representative figures were included (Figure 4.12 (a) and (b)).

The micrographs of etched thin-wall deposition reveal distinct microstructural features along the build height (Figure 4.12). The overall microstructure displayed distinct variations along the building direction.

At the bottom of the wall, corresponding to the first layer adjacent to the substrate, the microstructure consisted of more and finer directional columnar grains. The columnar grain alignment is strong, forming a well-defined directional structure in the building direction.

In the middle section of the thin-wall, which contains multiple intermediate layers, a repeating pattern is observed within each layer. Columnar grains predominantly extend in the building direction at the layer interface, marking the part where a new layer solidifies on the previously deposited material. When moving upward within the same layer, the columnar feature becomes progressively less distinct. Aside from the repeating pattern of directional columnar grains, it can be observed that grains in the higher layers are slightly coarser than those in the first layer, with a tendency to grow coarser with higher layer numbers.

At the top of the wall, corresponding to the uppermost/final deposited layer, the microstructure shows a more noticeable change in microstructural features within the layer. At the uppermost layer, a mixing of grain types can be observed from the bottom to the top of this layer, see Figure 4.13.

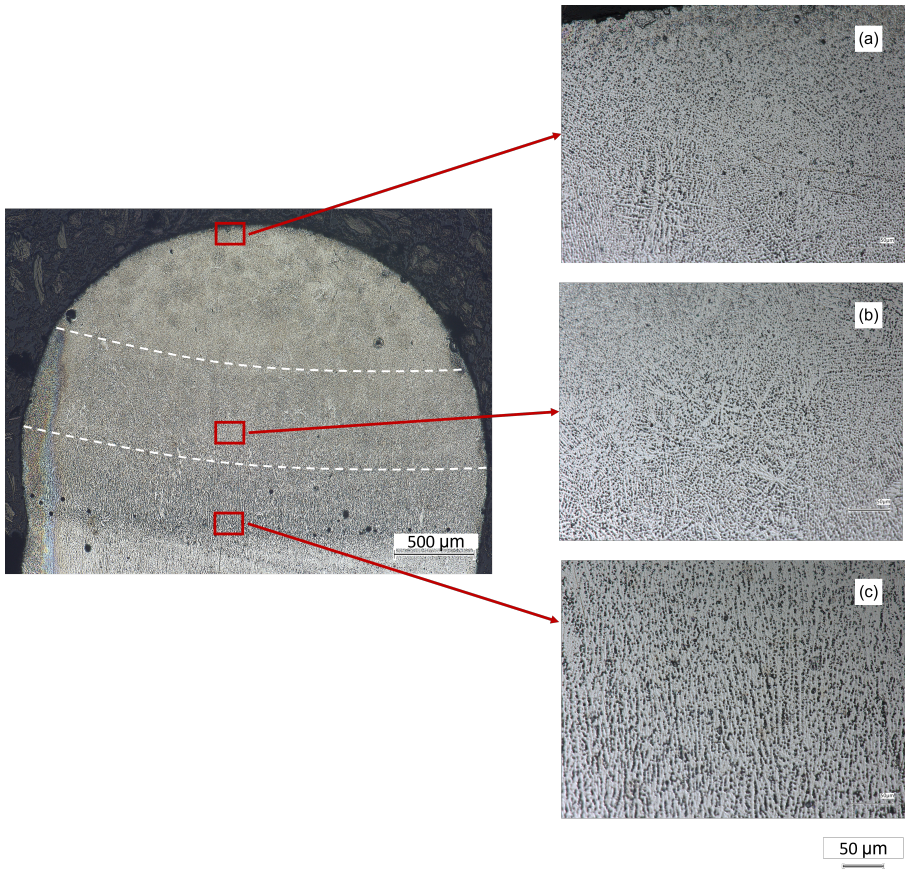

Figure 4.13: Micrographs of selected positions from the uppermost layer of a 6-layer thin-wall deposition. (The dotted lines separate the regions presenting different microstructural features.)

The bottom region of the final layer still exhibits columnar grains similar to those observed in lower layers, as mentioned in the previous paragraphs. However, in the mid-layer region, the columnar character breaks down and is replaced by irregular, equiaxed dendritic features, often observed as snowflake-like or branched grains. The distribution of the equiaxed dendrites has no preferential orientation. Near the layer crown of the final layer, these dendritic features remain present but appear more sparsely distributed compared to the denser arrangement observed below.

Overall, the microstructural evolution across the wall height and within each layer demonstrates a consistent pattern: columnar grains are dominant near solid–solid interfaces, while more irregular and equiaxed dendritic features appear toward the upper portions of the layers, particularly in the final deposition.

- **SEM and EDS Results**
  To investigate whether multilayer deposition leads to compositional changes, particularly expected Mg loss due to evaporation, SEM imaging and EDS analyses were conducted on the thin-wall structures. This analysis aimed to determine whether the higher porosity observed in thin walls could be associated with local depletion of Mg. No microstructural features indicative of severe Mg depletion (e.g., abnormal dendrite morphology or oxide films) were observed.

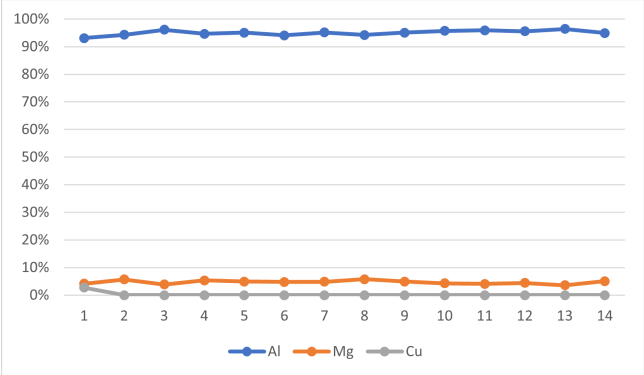

Figure 4.14: Compositional changes in Al, Mg and Cu in the thin-wall sample along the building direction.

To evaluate possible compositional changes throughout the thin wall, EDS point analyses were performed at representative regions: To begin with, an overview EDS analyses were conducted along the build height. A total of 14 EDS point measurements were taken along the height of the thin-wall to obtain an overview of the compositional variation from the substrate region to the top of the wall. Cu was detected only at the first point, located nearest to the substrate. Beyond this location, all remaining points showed a consistent Al–Mg composition (≈ 93–96 wt% Al and ≈ 4–6 wt% Mg), with Cu remaining below the detection limit of the system. This trend is illustrated in Figure 4.14, where the Cu content drops to 0 wt% after the first point and the Al and Mg contents remain quite consistent.

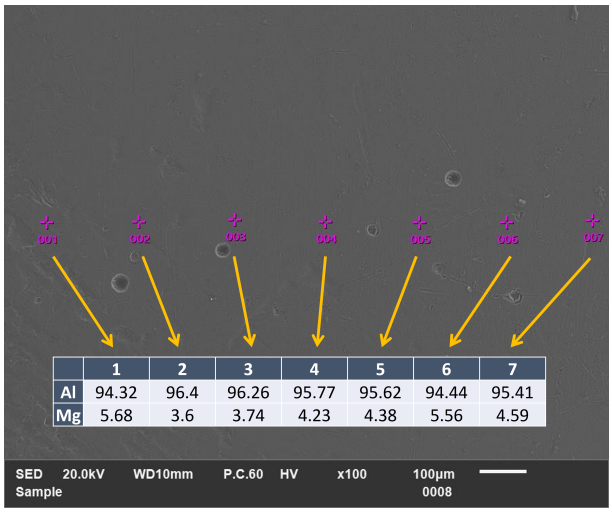

(a) Interlayer region that contains pores

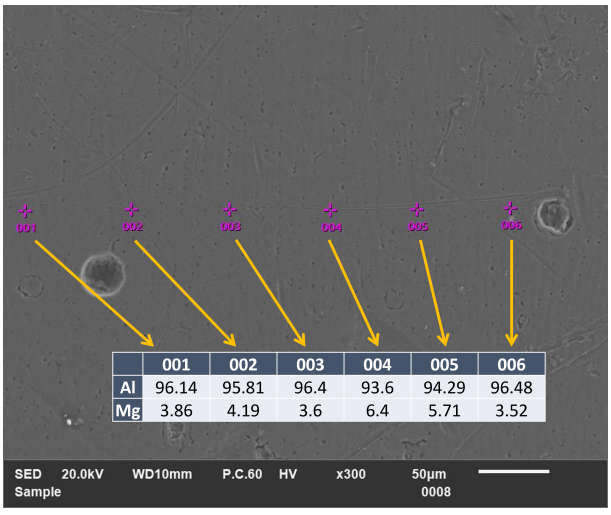

(b) An enlarged area of pore adjacency

Figure 4.15: SEM images and EDS measurements in the interlayer region and the enlarged pore-containing area.

Besides the measurements along the building direction, the interlayer region containing pores was focused on. Several points were measured horizontally to determine whether pores were associated with locally reduced Mg. Upon that, an enlarged region near the pores was investigated to have higher magnification

points taken to verify consistency. Across the selected locations, the measured Mg content ranged from approximately 3.5 to 6.7 wt%, which overlaps with the composition of the feedstock wire. No consistent trend of changes in Mg content in the thin-wall or the pore-containing interlayer regions was detected. The observed fluctuations fall within EDS measurement scatter and the expected microsegregation behaviour of Al-Mg alloys.

Overall, the EDS results do not indicate measurable evaporation of Mg during thin-wall deposition. Therefore, Mg loss is unlikely to be the dominant mechanism contributing to porosity formation in these samples.

- **EBSD Results**
  For details about the variation in grain size and their orientation, Electron Back Scattered Diffraction (EBSD) analysis was carried out for two selected thin-wall samples (TW3 and TW4). Inverse pole figure (IPF) maps and image quality (IQ) maps for TW3 and TW4 are shown in Figure 4.16 - 4.18. EBSD analysis was performed on selected regions of the thin-wall samples. For each sample, two areas were scanned: a TOP region close to the upper surface of the wall, and a BOT region located near the substrate/fusion line. These regions were chosen to capture microstructural differences that may arise along the build direction. From the IPF maps, the overall differences in grain size and grain orientation distribution can be observed. These qualitative differences are confirmed by quantitative grain-size values, obtained using the line-intercept method. Three horizontal and three vertical lines were taken on each EBSD map, and the number of grain boundaries intersecting each line was counted. Grain size was then calculated using d=L/N, where L is the line length, and N is the number of boundary intersections.

Table 4.2: The distortion measurements and the normalised distortion in two different directions (XZ and YZ) for thin-wall samples.

Sample	Average grain width (μm)	Average grain height (μm)	Aspect ratio (W/H)
TW 3 (BOT)	17.15	59.41	0.2888
TW 3 (TOP)	61.54	207.53	0.2966
TW 4 (TOP)	41.12	151.38	0.3113

  - **6-Layer Sample (TW4)**
    Figure 4.16 shows the EBSD IPF map of the top section from a 6-layer thin-wall. The microstructure

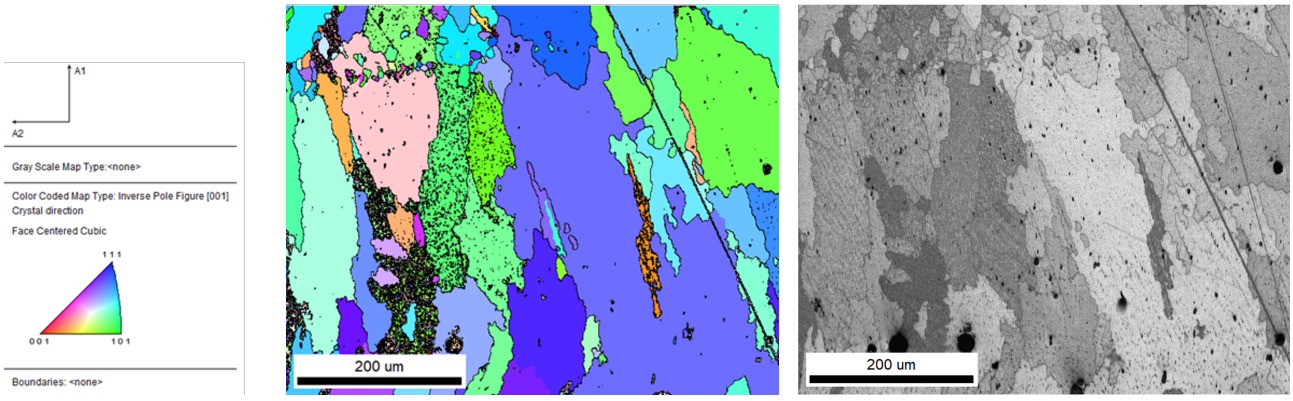

Figure 4.16: EBSD inverse pole figure (IPF) map and image quality (IQ) map of top section of a 6-layer thin-wall sample (TW4).

    is characterised by large, elongated columnar grains aligned predominantly in the build direction. In addition, the orientation distribution of the grains is dominated by blue, green, and purple colours, corresponding primarily to <101> and <111> crystallographic orientations. Only with very few orange grains are exhibited, and no <001> grains are observed. Other than that, small, intermittent equiaxed grains are present near interlayer boundaries, contrasting with the surrounding predominant coarse columnar grains. The 6-layer sample scan contained only a small number of fully captured grains due to their large size and the limited field of view. As a result, only approximate grain size values could be obtained and are summarised in Table 4.2. No directional trend was evident.

  - **12-Layer Sample (TW3)**
    Figure 4.17 shows the EBSD IPF map acquired from the TOP region of the 12-layer thin-wall. The

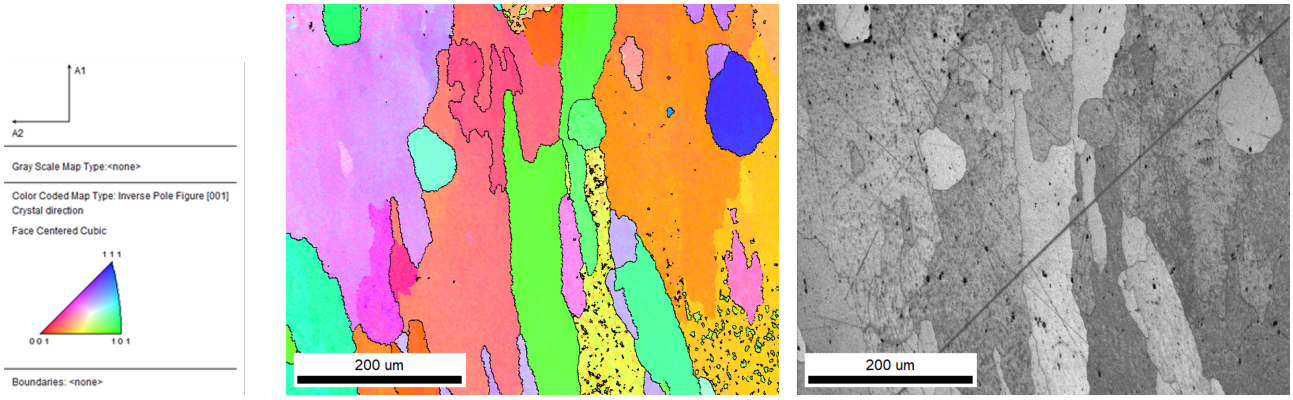

Figure 4.17: EBSD inverse pole figure (IPF) map and image quality (IQ) map of top section of a 12-layer thin-wall sample (TW3).

microstructure in this region is dominated by large, elongated grains with long axes approximately aligned with the build direction. Compared to the BOT region of the same sample, the TOP area displays significantly coarser grains. Meanwhile, compared to the TOP map of the 6-layer sample, the grains in this 12-layer TOP map are also visually larger.

The IPF colour distribution in the 12-layer TOP is leaning toward warmer hues (red-orange–yellow), indicating a relative dominance of orientations associated with <001>. In contrast, blue tones are rarely spotted, indicating a lack of orientation in <111>. Because many grains are only partially contained within the scanned field of view, only approximate statistics are presented; measured grain-size values are summarised in Table 4.2.

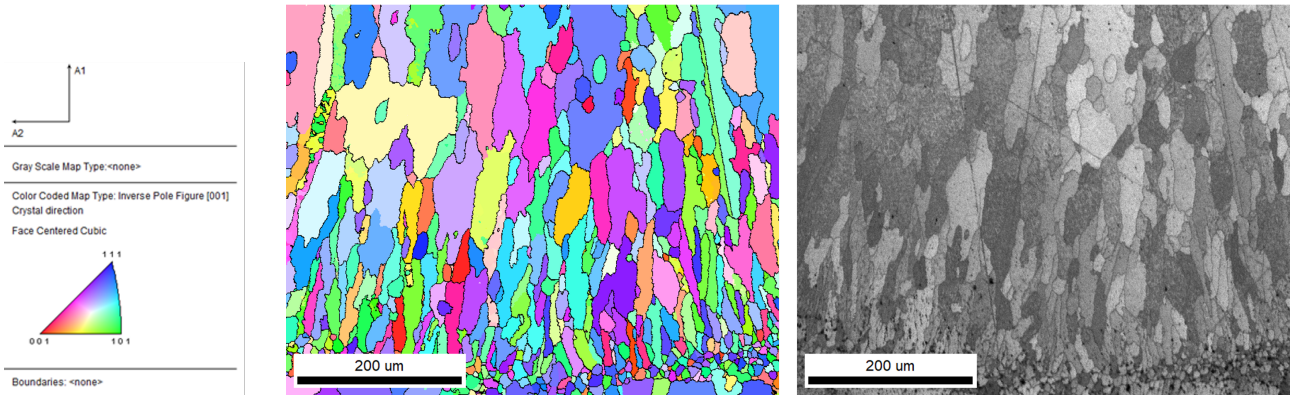

Figure 4.18: EBSD inverse pole figure (IPF) map and image quality (IQ) map of bottom section (near the fusion line) of a 12-layer thin-wall sample (TW3).

Figure 4.18 shows the EBSD IPF map of the region near the substrate in a 12-layer sample. The grains distributed close to the fusion line are significantly finer than the upper regions. A visible transition exists from fine equiaxed grains near the substrate to elongated grains upward. The grains farther from the fusion line have a gradual but small increase in size, and they also become more elongated. However, overall remain smaller and less continuous compared to the 6-layer TOP sample. Aside from the grain size, the colour distribution displays a wide range of colours. This suggests a more random pattern, with no dominant orientation. For the 12-layer sample, the horizontal grain-intercept measurements showed a clear increase from the bottom region toward the top of the wall. Figure 4.19 presents the average grain widths from the three horizontal lines, confirming the visual impression from the IPF map. Grain size increased from 10.8μm at the bottom line to 29.1μm at the top line.

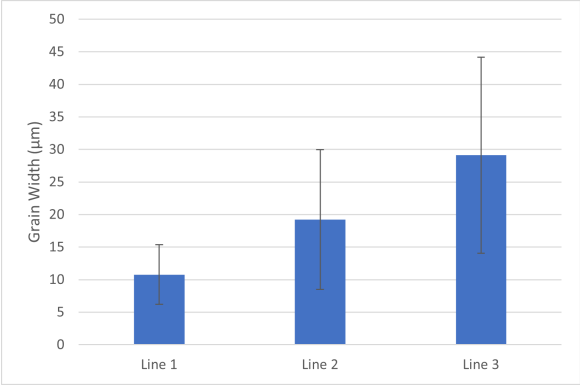

Figure 4.19: Average grain size for each horizontal line taken from the TW3 EBSD scan.

4.2.3 Distortion Analysis

As detailed mechanisms discussed in Chapter 2, due to the local thermal gradients, expansion and shrinkage, residual stresses are introduced. Thermal distortion arises from non-uniform heat distribution and constrained thermal contraction during solidification, leading to residual stress accumulation and substrate bending. After completion of the build, the distortion became observable after releasing the sample from the clamping system.

Distortion measurements obtained from 3D scans are summarised in Table 4.3. Distortion was quantified along both the longitudinal (15 mm) and transverse (5 mm) directions of the substrate. For the transverse direction, distortion was further evaluated by averaging over ten cross-sections taken along the wall length. The distortion values and normalisation for both directions are summarised in Table 4.3.

Table 4.3: The distortion measurements and the normalised distortion in two different directions (XZ and YZ) for thin-wall samples.

Sample	Number of Layers	Travel Speed	Distortion XZ	Normalised XZ	Distortion YZ	Normalised YZ
TW1	6	20	0.404	1.62%	1.35	1.80%
TW2	7	20	0.463	1.85%	1.70	2.26%
TW3	12	20	0.588	2.35%	1.98	2.64%
TW4	6	15	0.527	2.11%	1.74	2.32%
TW5	12	15	0.796	3.18%	2.75	3.67%
TW6	6	15	0.569	2.28%	1.74	2.32%

In all samples, distortion values increased with the number of deposited layers, suggesting a cumulative build-up effect of thermally induced stresses. The raw mid-span deflection ranged from 0.404 mm for a 6-layer wall to 0.796 mm for a 12-layer wall in the short-side direction, and from 1.350 mm to 2.750 mm in the long-side direction. Regardless of layer number, distortion was consistently more pronounced along the longitudinal direction of the substrate compared to the transverse side.

To minimise the difference in the lengths of the substrate sides, normalisation was taken. After normalisation to account for differences in span length, the long-side deflection remained slightly higher (1.80–3.67%) than that measured on the other side (1.62–3.18%).

Notably, the highest distortion was observed in the 12-layer wall deposited at a lower travel speed, reaching a normalised deflection of 3.67% along the long direction.

For the transverse side of the substrate, distortion values were obtained from ten cross-sections along its span. The distortion measurements taken along the wall length indicated a slight increase in displacement at the mid-wall region, while lower values were recorded near the start and end positions (Figure 4.20. Although the magnitude of this variation is small, This trend was consistent across all the thin-wall samples.

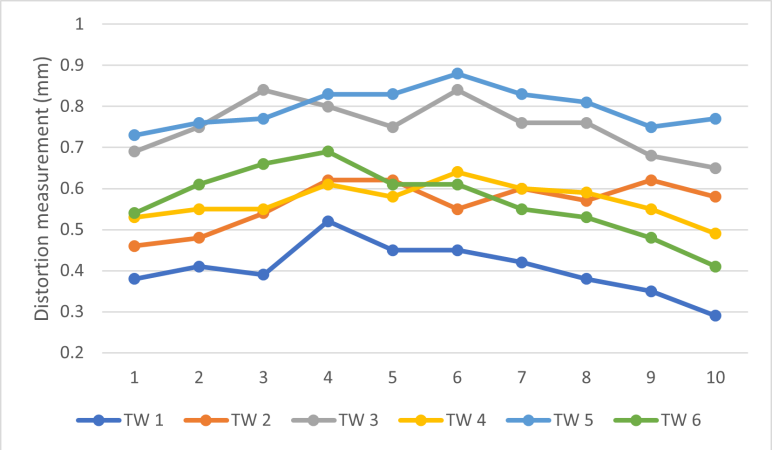

Figure 4.20: Distortion measured at ten positions along the length of each thin-wall sample.

4.2.4 Porosity Analysis

In multi-layer depositions, the porosity was more severe than that of single-track depositions. The porosity of the multi-layer thin walls was quantified from cross-sectional images to evaluate the influence of build height and travel speed on pore formation (Table 4.4).

Table 4.4: The porosity measurements for thin-wall samples.

Sample	Number of Layers	Travel Speed (mm/s)	Porosity Ratio
TW1	6	20	0.69%
TW2	7	20	0.83%
TW3	12	20	1.26%
TW4	6	15	0.63%
TW5	12	15	0.92%
TW6	6	15	0.71%

The porosity was calculated for the porosity ratio, determined as the ratio between the total pore area and the total cross-sectional area of the printed wall (excluding the substrate). Overall, across all samples, porosity remained below 1.5%.

The porosity ratio increased with the number of deposited layers, indicating that samples with greater build height contained a higher volume fraction of pores. The pores were predominantly located along the boundaries between successive layers; the pores were distributed more densely around the interlayer region. A lower travel speed was generally associated with a slightly reduced porosity compared to a higher travel speed under other fixed conditions.

For the 12-layer sample deposited at a travel speed of 15 mm/s, multiple cross-sections were examined. Particularly, one cross-section exhibited a markedly higher porosity than all others, even higher than that of the higher-speed depositions, while the remaining sections showed considerably lower pore fractions. This suggests that the porosity distribution may vary locally within the same thin-wall in the longitudinal direction, rather than being uniform across its length.

4.2.5 Hardness Test

The microhardness distribution of the cross-sections of the thin-wall samples along the building direction was measured, as shown in Figure 4.21. The microhardness in the transitional region from the substrate to the first deposited layer was measured to be higher than that of the rest deposited part. The values measured adjacent to the substrate of the thin-wall presented slightly higher numbers. Other than that, the values obtained across the building direction were relatively uniform, with no significant fluctuations. An average was taken across all indentations, with a value of 76.2 HV.

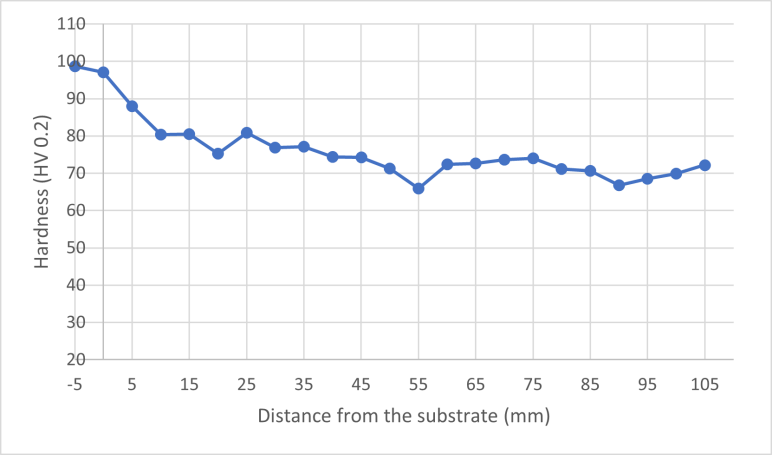

Figure 4.21: The hardness tests measured along the building direction of a 12-layer thin-wall sample (TW5).

4.2.6 Thermal Analysis

The temperature history obtained during a 5-layer thin-wall deposition was summarised into a diagram, see Figure 4.22. The blue curve (Thermocouple 1) shows the record from the thermocouple attached closer to the deposition, and the orange curve (Thermocouple 2) suggests the other one placed further from the deposition. The exact measuring locations were shown in Figure 3.10. The plots exhibit five distinct thermal cycles with a peak followed by a plateau, each corresponding to one layer deposited. Also, peak temperatures decrease progressively from the first to the last deposition for both thermocouples. Thermocouple 1 recorded peak temperatures of 222.1 - 186 °C, while Thermocouple 2 recorded 132.5 - 120 °C. Thermocouple 1 consistently recorded higher peak temperatures than the far thermocouple, as expected from its location closer to the melt pool. In addition, a measurable delay between the two peak temperatures was observed in every cycle; this delay ranged from approximately 1 to 1.3 seconds.

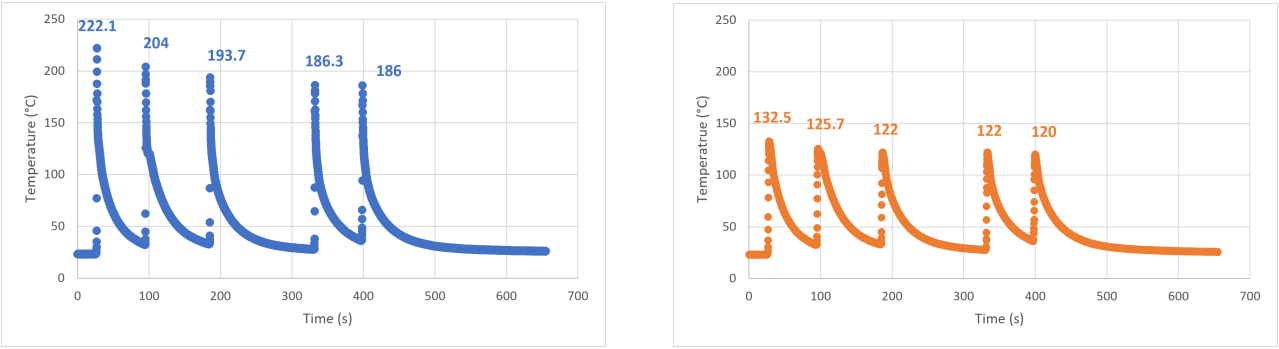

(a) Thermocouple 1

(b) Thermocouple 2

Figure 4.22: The temperature profiles of two thermocouples during a 5-layer deposition.

The heating and cooling rates were calculated for both thermocouples across all five cycles. Figure 4.23 (a) presents the heating rates for both thermocouples across the five cycles, while Figure 4.23 (b) shows the corresponding cooling rates. While the absolute values differ between the two thermocouples, both sets of measurements exhibit cycle-to-cycle variations associated with differences in pre-pass temperature. On the one hand, heating rates present the highest in cycles 2–3 and gradually decrease during later cycles. On the other hand, cooling rates remained relatively stable across cycles, exhibiting more consistency than large changes or fluctuations, with Thermocouple 1 showing significantly higher values than Thermocouple 2.

4.2.7 XRD Analysis

Figure 4.24 shows the two-dimensional XRD diffraction ring patterns obtained from the deposited material. Two datasets were collected: one without sample oscillation (the upper picture) and one with oscillation during exposure (the lower picture).

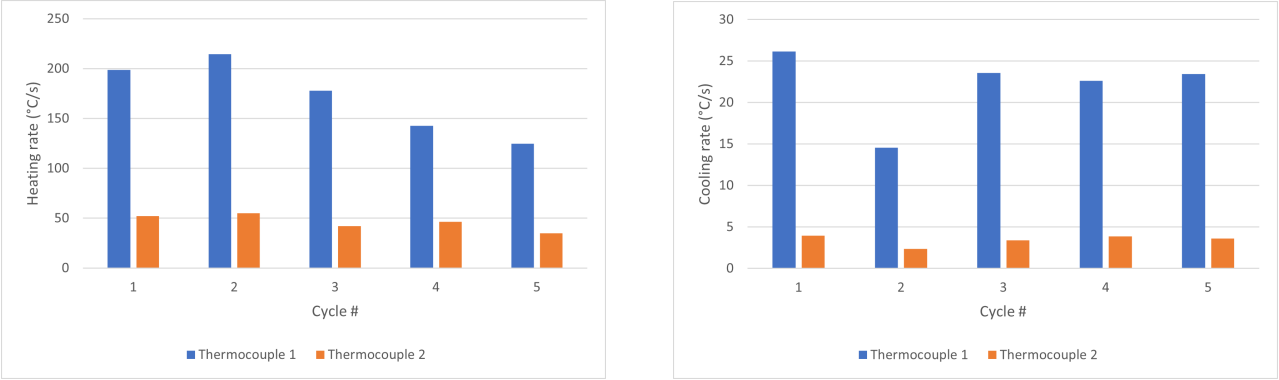

(a) Heating rates

(b) Cooling rates

Figure 4.23: The heating rates and cooling rates of two thermocouples for each cycle during a 5-layer deposition.

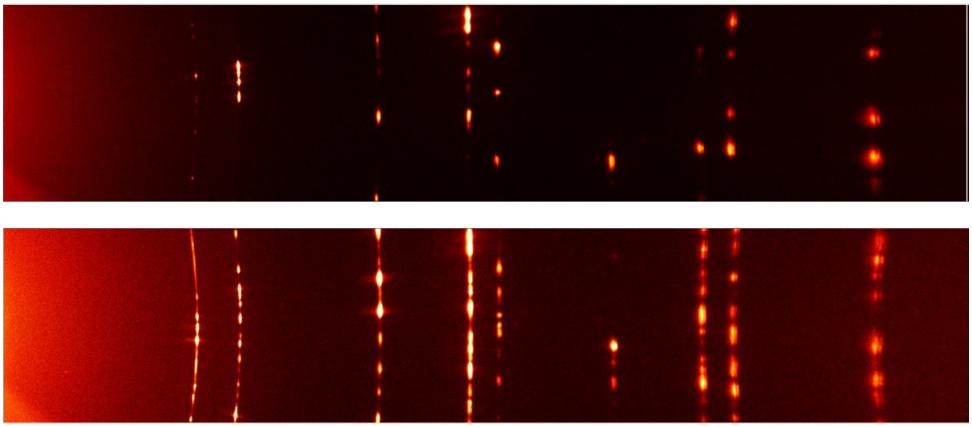

Figure 4.24: 2D diffraction ring patterns obtained from the thin-wall sample (TW3). The upper figure is without oscillation, while the lower figure presents patterns with oscillation.

In the pattern obtained without oscillation, the diffraction rings appear as discrete and dotted rather than fully continuous rings. Such discontinuities are typical when large grains and strong crystallographic texture are contained, as only a limited number of crystallites satisfy the condition at a fixed sample orientation. This behaviour is consistent with the coarse, directional grain structures exhibited in LDED depositions.

When the sample is measured with oscillation, the rings become more continuous. Oscillation increases the number of diffracting grains and effectively averages out preferred orientation effects. As a result, each ring is more evenly distributed, providing improved counting statistics.

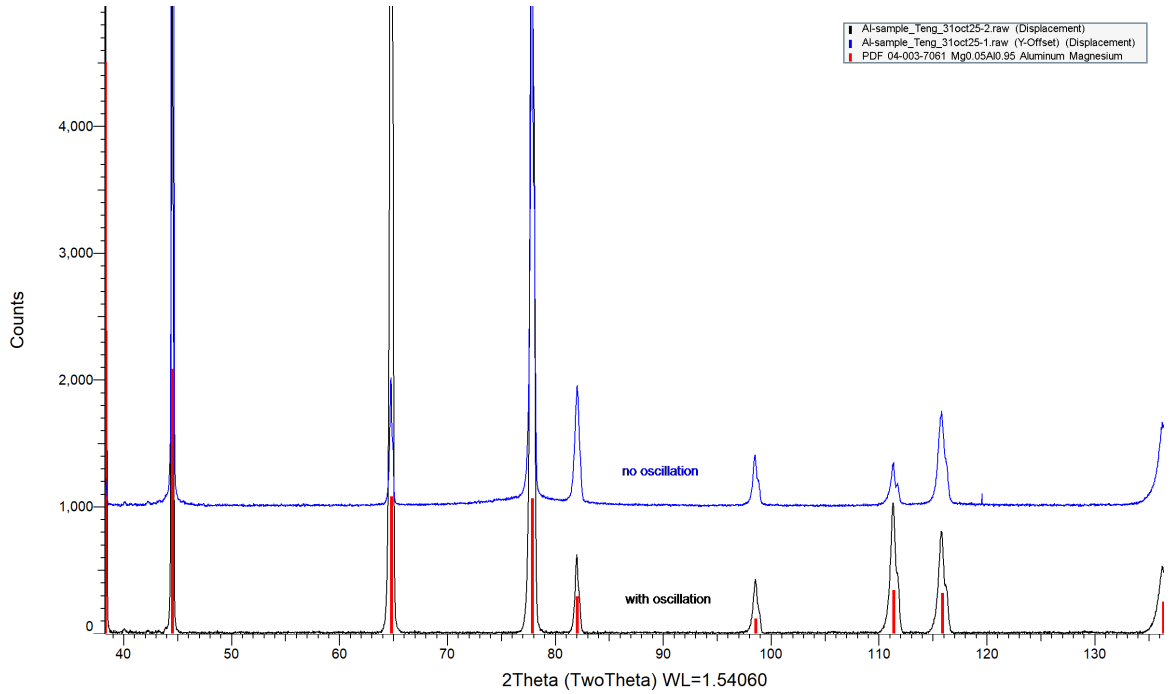

Figure 4.25: XRD diffraction peak profile of the thin-wall sample (TW3). An intensity offset was applied to the dataset of no oscillation for clarity.

In this work, the XRD pattern (Figure 4.25 shows a distribution of major peaks that resembles that of Al. It does not show clear additional peaks that can be associated with intermetallic phases.

The peak positions were used to calculate the d-spacings via Bragg's law, and thus the lattice parameter (a) was derived for each reflection, assuming an FCC crystal structure. The calculated values are summarised in Table 4.5. Using Bragg's law and standard cubic indexing, the measurable reflections give a mean lattice parameter of a = 4.0672 ± 0.0013 Å. The calculated lattice parameters show alignment with the reference number for aluminium ($a_{ref} \approx 4.049$ Å), with a slightly larger averaged a-value in the present material. The deviation shows a consistently larger value across all peak positions ($\Delta a \approx +0.42$ to $+0.53$ %), indicating a uniform lattice expansion.

Table 4.5: Measured 2θ positions, calculated d-spacings and lattice parameters for diffraction peaks obtained from the thin-wall sample. Reference values for Al are included for comparison. (Δa denotes the deviation of the calculated lattice parameter from the reference value.)

Peak	2θ (°)	d-spacing (Å)	Assigned (hkl)	a (Å)	$2-\theta_{ref}$ (°)	d_{ref} (Å)	a_{ref} (Å)	Δa (%)
1	38.28	2.349	(111)	4.0678	38.47	2.338	4.0495	0.45
2	44.49	2.035	(200)	4.0696	44.74	2.024	4.0480	0.53
3	64.80	1.438	(220)	4.0661	65.13	1.431	4.0475	0.46
4	77.78	1.227	(311)	4.0693	78.23	1.221	4.0496	0.49
5	82.02	1.174	(222)	4.0673	82.44	1.169	4.0495	0.44
6	98.52	1.017	(400)	4.0666	99.08	1.012	4.0496	0.42
7	111.33	0.933	(331)	4.0662	112.04	0.929	4.0490	0.42
8	115.80	0.909	(420)	4.0666	116.57	0.906	4.0495	0.42

Chapter 5

Discussion

This chapter discusses the influence of process parameters and the number of layers on different aspects, such as deposition geometries, microstructural features, thermal history, as well as defect formation in multi-layer depositions, including porosity and distortion.

5.1 Single-Bead Depositions

5.1.1 The Effect of Process Parameters on Bead Geometries

This section discusses the influence of process parameters on the geometrical characteristics and structural integrity of single-bead depositions. The influence of process parameters on single-bead geometry is first summarised to establish the fundamental relationship between each parameter and bead shape characteristics. The results obtained in Chapter 4 are consolidated in Table 5.1 to give an overview on the main trends.

Table 5.1: Summarised trend of the effect of increasing parameters on bead geometry.

	Bead Width	Bead Height	Aspect Ratio	Contact Angle	Penetration Depth
Laser Power	↑	↓	↓	↓	↑
Travel Speed	↓	↓	↓	↓	↑
Wire-Feeding Rate	↓	↑	↑	↑	↓

- **Wire-Feeding Rate**
  With increasing wire-feeding rate, the bead geometry showed systematic changes. Since laser power and travel speed were fixed, adding more feedstock material per unit energy results in a relatively lower heat available for substrate melting and the horizontal spreading of the deposition. As a result, the bead width decreased while the bead height increased, thus giving rise to a larger aspect ratio.

  Correspondingly, the contact angles increased, presenting a taller bead shape. Furthermore, the penetration depth decreased, as a larger portion of the laser energy was consumed in melting the wire fed rather than being received by the substrate to form a deeper melt pool. These combined trends indicate that higher wire-feeding rates promote bead build-up above the substrate but limit substrate dilution.

  The fixed laser power was chosen to realise the melting of the wire at the maximum wire-feeding rate that can be obtained in this setup. The wire-feeding rate was limited by the wire-feeder used in the experiments, to an upper limit of 4.25 m/min. If it were possible to increase the wire-feeding rate further, the process would become unstable, and part of the wire would be delivered in a non-molten state. Otherwise, a higher laser power needs to be considered.

- **Travel Speed**
  Raising the travel speed at a constant wire-feeding rate and laser power, the deposited beads were shown to become narrower and shallower. Compared to the bead width, the bead height decreased rather slightly, leading to a lower aspect ratio with increasing speed. However, at 30 mm/s, bead height increased unexpectedly, leading to a spike in aspect ratio. The anomalous aspect ratio at 30 mm/s likely results from instability that occurred during deposition. At this speed, the reduced energy input may have been insufficient to maintain a stable bead profile, leading to local irregularities. While bead width and height

individually showed only minor deviations, the effects from both combined amplified the deviation in aspect ratio.

The contact angle was reduced, which shows consistency with a flatter and more spread-out bead profile. The reduced penetration depth indicates that less energy was delivered per unit length of the track, leading to a smaller and less deeply fused melt pool. Physically, this trend reflects the lower specific energy input associated with higher traverse speeds. While faster travel improves productivity, excessive speed may limit the stability in the process and compromise the bonding between depositions.

- **Laser Power**
  The track deposited with a travel speed of up to 30 mm/s showed significant inconsistency, suggesting there was less heat focused on the material per unit time or unit length, and the melt pool cannot remain in a consistent way. As a result, in order to supply sufficient heat to give a stable melt pool at such a travel speed, the laser power should be elevated.

  At constant travel speed and wire-feeding rate, increasing laser power enhanced both bead width and penetration depth. The bead height showed a modest increase, but the aspect ratio decreased slightly because the lateral spread was more pronounced. Contact angle values were reduced, consistent with flatter bead profiles formed at higher energy input. The greater melt pool volume and depth reflect the stronger substrate dilution achieved with more available heat. This indicates that higher laser power promotes improved fusion between the bead and substrate, although at the expense of greater dilution and potentially wider heat-affected zones. Hence, a careful control of laser power is required to balance penetration with geometric precision.

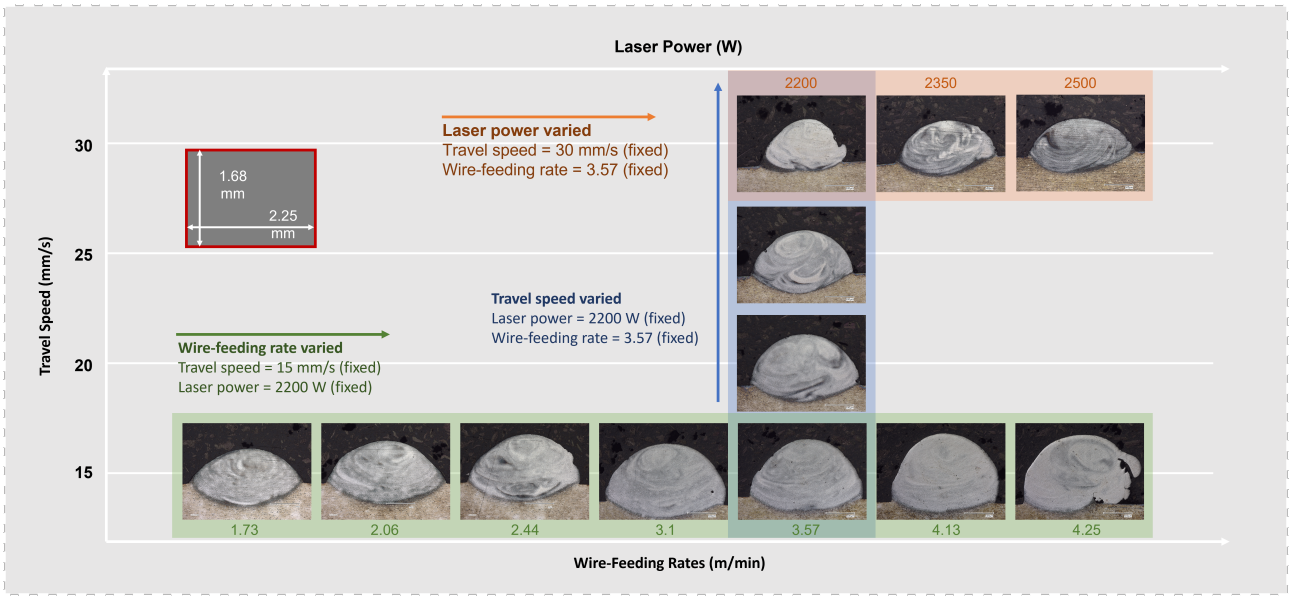

Figure 5.1: The overview of cross-sections of single-bead depositions with varied parameters.

In summary, the geometrical evolution of single-bead tracks is governed by the interplay between energy input and material supply. A higher wire-feeding rate promotes bead build-up but reduces substrate dilution, whereas greater laser power enhances penetration and lateral spreading through higher melt-pool temperatures. Increasing travel speed diminishes both width and depth due to reduced specific energy input, and at excessive values may destabilise the deposition.

These trends suggest that process optimisation for stable bead geometry requires balancing the volumetric energy density and feed rate: sufficient to ensure continuous melting and substrate fusion, but not excessive to the extent of over-widening or deep dilution. Within the studied parameter ranges, the results indicate that a moderate wire-feeding rate combined with intermediate travel speed and laser power provides the most favourable conditions for obtaining a uniform bead with adequate bonding and geometric precision—serving as a guideline for subsequent multi-layer deposition.

Across all the single-bead depositions, two tracks exhibit relatively better quality in terms of high aspect ratio, consistency in deposition, and smoothness of the track. The parameter sets used for the depositions were therefore selected to perform vertical building.

5.1.2 Microstructure Analysis

In the single-bead depositions, the irregular contrast observed after etching likely corresponds to orientation-dependent etching behaviour. Considering the EDS point measurements, the lighter/darker region can be linked to the difference in compositional distribution.

The alternating lighter and darker regions observed after etching indicate subtle microstructural or compositional variations within the single-bead deposition. The EDS results suggest that these contrast variations correspond to minor changes in alloy composition, particularly involving Cu and Mg.

The darker regions, which matched the composition of the feedstock wire, likely represent areas with minimal elemental redistribution during solidification. In the lighter regions, Cu was detected alongside a small reduction in Mg, which may indicate localised dilution effects. The presence of an average 3.8 wt% of Cu can be attributed to dilution from the substrate (with $\approx$ 6.39 wt% Cu). During the initial deposition, the laser melts a portion of the substrate together with the feedstock wire, allowing Cu from the base alloy to mix into the melt pool. This results in a locally higher Cu content in the solidified bead.

If the bead geometry or thermal field promotes limited mixing with substrate material containing trace Cu, incorporation of Cu into near-interface regions will occur. Although the EDS traces are small, even low-level diffusion or mechanical mixing can be sufficient to modify the local etching response.

5.1.3 Porosity

Single-bead depositions exhibited negligible porosity. Across all cross-sections, only one or two isolated pores were observed, typically located near the track edge. The overall absence of pores is consistent with the relatively simple thermal cycle and the stable conditions during a single pass, where gas bubbles can readily escape before solidification. Because porosity does not manifest clearly at the single-bead level, the mechanisms responsible for pore formation are therefore discussed in greater depth for the multi-layer depositions.

5.2 Multi-layer Deposition

Building upon the single-bead depositions, this section discusses the phenomena observed during multi-layer depositions. As additional layers are stacked, thermal accumulation, remelting, and residual stress development become significant. The following sub-sections address how these effects manifest in terms of shape evolution, porosity, and substrate distortion.

5.2.1 Shape Evolution and Dimensions

Based on the single-bead depositions, parameter sets can be obtained to build thin-wall structures. The conditions selected from the single bead experiments resulted in a stable track and relatively smoother quality along the deposition, at travel speed of 15 and 20 mm/s, with a constant wire-feeding rate of 3.57 m/min. However, boundary conditions will start to deviate when the distance to substrate increases. The geometry of multi-layer structures evolves as additional layers are deposited, primarily due to heat accumulation and layer remelting. Consequently, the power is gradually reduced (2200 W $\rightarrow$ 2100 W $\rightarrow$ 2000 W in the early layers) with increasing distance to the workpiece to avoid too high a heat accumulation in the deposit.

- **Shape Evolution**
  The irregular shape of the thin-walls observed at the beginning and end of the walls is attributed to the transient conditions during process initiation and termination. The manual synchronisation of wire-feeding and workpiece movement likely caused a temporary mismatch in consistency, producing overfilled or underfilled regions. The accumulation and the lack of the feedstock material at the initiation and the termination of the deposition were also reported by others [42] based on different deposition strategies.

  Across all thin-wall samples, the first deposited layer consistently exhibited a smaller width than subsequent layers. This behaviour can be explained by the higher thermal conductivity of the substrate, which leads to rapid heat dissipation into the substrate and limited melt pool spreading during the initial stage of the deposition. As the deposition proceeds, heat accumulation increases the substrate temperature, also the wall builds higher, putting distance between the deposition and the substrate. This promotes wider bead spreading, hence giving a wider and more uniform bead formation in the upper layers. Afterwards, the wall width remained relatively constant, suggesting that the process achieved a steady melt pool width after the first few layers.

- **Dimensions**
  The dimensional measurements show that higher travel speed produced taller but narrower walls, while lower travel speed resulted in wider yet slightly shorter walls. These differences correspond to variations in the melt pool volume and solidification rate under different heat inputs. Also, the results reflected similarly with the single-bead deposition.

Overall, the observations show that achieving dimensional consistency in multi-layer walls requires stable control over the deposition process. The irregularities at the intial and terminal position of the depositions highlight the sensitivity of geometry to transient conditions such as start–stop synchronisation. The narrower first layer indicates how cooling rates affect the melt pool size and thus the resultant deposition dimension. Maintaining steady wire feeding, precise laser–wire alignment, and controlled travel speed are therefore essential to obtain uniform wall geometry throughout the build.

5.2.2 Microstructure Characterisation

- **OM Results**
  The etched micrographs reveal the typical grain morphology associated with DED processes, reflecting strong directional solidification governed by the local thermal gradient and solidification rate.

  For multi-layer depositions, the columnar grain structure is spotted through multiple layers, especially at the interlayer region, where the new layer solidifies on the previous layer. In addition, the finer-grain features observed near the substrate than in higher layers result from higher cooling rates and can be explained by the heat sink effect due to the proximity to the substrate.

  At the uppermost layer, since the influence of the subsequent layer does not exist, a complete layer can be observed. The transition of microstructural features to equiaxed grains and clear dendritic features suggests a different solidification mechanism with the lower layers, and can be correlated to faster cooling. The faster cooling stems from the direct contact and sufficient exposure of the last deposited layer to the air.

- **SEM and EDS Results**
  The EDS results do not indicate systematic changes in the composition along the building direction, nor in the interlayer region. Suspected depletion of Mg in the bulk of the thin-wall samples was not detected, suggesting that alloy evaporation is unlikely to be the dominant contribution to pore formation for the tested parameter sets. Local O contamination found in a small fraction of points may indicate surface oxide fragments or polishing/handling contamination.

  In contrast to the single-bead depositions, in the thin-walls, dilution of Cu becomes negligible beyond the first layer, as subsequent layers are deposited on previously solidified material rather than on the substrate. This explains why Cu was only detected in the region closest to the substrate and remained below the detection limit in the remaining part of the wall.

- **EBSD Results**
  The EBSD results reveal clear differences in grain morphology and orientation between samples deposited under different process conditions and at different heights within the thin walls. All scans show elongated grains aligned approximately parallel to the build direction, consistent with the solidification governed by the directional thermal gradient characteristic of DED processes.

  A comparison between the 6-layer and 12-layer samples reveals how grain size is governed not only by the processing parameters but also by the total number of deposited layers. In the two TOP-region scans, both taken in the upper portion of the thin-walls, TW3 (processed at a higher travel speed/lower heat input) exhibits larger grains than TW4 (processed at a lower travel speed/higher heat input).

  Considering the heat input solely, a lower heat input generally leads to faster cooling and consequently finer grains. However, the higher number of layers of the 12-layer sample is also considered as a potential factor in reducing its cooling rate. As the number of layers goes up, the distance to the substrate increases, and the heat accumulation builds up. With less heat dissipation to the substrate and the heated-up previous deposition layer, they collectively lead to a slower cooling rate and therefore affect the grain size. While the observed differences between the two TOP scans can be associated with heat input and build height, the capture of EBSD maps on only a limited field of view should also be acknowledged. The large grain sizes in the TOP regions mean that only a small number of grains are fully captured in each scan. Therefore, the comparison should be interpreted with caution and regarded as a local observation rather than a global representation of the entire sample.

Overall, the EBSD results demonstrate that both heat input and build height influence solidification and grain size in thin-wall structures. A higher input and a higher number of layers lead to a slower cooling rate and grain coarsening in the upper layers. In contrast, the proximity to the substrate favours the development of finer grains. The combined influence of process parameters, build height, and local thermal history explains the observed variations in grain size and texture between the scanned regions.

The EBSD observations of coarse grains and mild crystallographic texture in the top regions of both specimens are consistent with the XRD ring pattern. The non-oscillated diffraction rings exhibit a spotty and intermittent appearance, which typically indicates either large grain sizes or pronounced preferred orientations. The concurrence of EBSD and XRD findings therefore strengthens the conclusion that the upper layers of the deposits possess coarser grains and some degree of texture.

5.2.3 Distortion Analysis

All depositions were performed under clamped conditions, which constrained thermal expansion during processing. As a result, residual stresses accumulated within the thin wall and the substrate. Once the samples were unclamped after deposition, these stresses partially relaxed, leading to the measured distortion. The clamping condition thus plays an essential role in the magnitude and manifestation of distortion.

Distortion increases with both the number of deposited layers and the lower travel speeds. The increase in deflection with the number of layers is consistent with the progressive heat accumulation and residual stress build-up expected in the multi-layer deposition processes. In addition, the effect of travel speed was evident: walls printed at 15 mm/s consistently showed greater distortion than those at 20 mm/s. The results from different travel speeds reflect that lower travel speeds introduce higher energy input per unit length, producing a larger melt pool and consequently greater shrinkage upon solidification.

Except for the effect of the number of layers and the travel speeds, distortion was observed consistently higher in the longitudinal direction than in the transverse direction.

The more pronounced distortion along the longitudinal direction aligns with the deposition path. This can be attributed to the larger amount of material deposited along this direction and the longer thermal path over which heating and cooling occur. The longitudinal axis therefore experiences a greater total contraction during solidification and subsequent cooling, explaining the larger distortion compared to the transverse direction. After the normalisations are taken, the directional differences remained, suggesting that the underlying mechanism is not purely geometric but tied to intrinsic thermal-mechanical interactions during deposition.

No cracks or delamination were observed in any of the samples. This indicates that despite the increases in distortion with build height and heat input, the resulting residual stresses remained below levels that lead to the initiation of cracking.

5.2.4 Porosity Analysis

Porosity is a critical defect affecting mechanical performance and density in additive-manufactured parts. As discussed in Chapter 2, pores may originate from gas entrapment or insufficient fusion between layers. As also experienced during welding processes, aluminium alloys are prone to porosity. Careful preparations are often required to avoid excessive pore formation, and this is also the case in additive manufacturing of aluminium alloys.

- **Melt Pool Flow Mechanism and Pore Behaviour**
  The behaviour of pores within the molten pool is governed by the melt pool flow and influenced by several interacting forces. Among them, Marangoni convection driven by the surface energy gradient, and buoyancy forces play the key roles in the escape of pores in the pool. Both Marangoni-driven convection and buoyancy forces act collectively on gas pores within the melt pool.

  The Marangoni effect creates a circulating flow pattern that moves molten metal outward and downward along the melt pool boundary before recirculating in the centre, see Figure 5.2. Gas pores in the liquid are carried along with this flow. Meanwhile, buoyancy provides an upward driving force and causes pores to float toward the upper region of the melt pool. Pores that reach the melt pool surface may escape, bursting into the atmosphere before the solidification is fully complete.

  Marangoni flow direction depends fundamentally on the sign of the surface-tension temperature coefficient ($d\sigma/dT$). In aluminium systems, $d\sigma/dT$ is negative, resulting in outward Marangoni flow. The surface-active elements cause changes in the surface tension, altering the flow pattern in the melt pool. At sufficiently high concentrations of the surface-active elements, the reversal of Marangoni flow is possible and causes an inward convection.

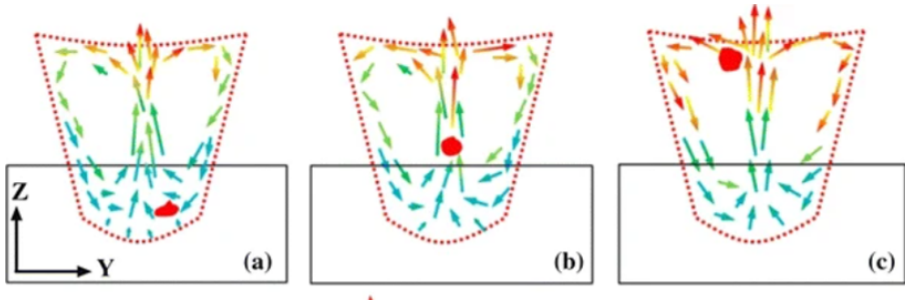

Figure 5.2: Schematics of Marangoni flow and the motion of a gas bubble in the circulating flow[43]. (The red dot in the figure indicates the gas bubble.)

The presence of surface-active elements, such as oxygen, can reduce the magnitude of this negative slope. This behaviour is illustrated in Figure 5.3, suggesting that the surface tension of liquid aluminium decreases with increasing temperature for various oxygen contents, producing a negative surface tension gradient that drives outward Marangoni flow. As the concentration of surface-active elements increases, this gradient becomes less negative.

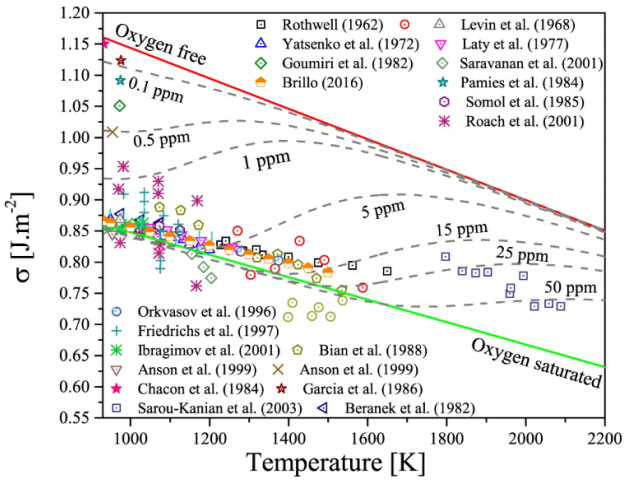

Figure 5.3: Predicted surface tension of liquid aluminium as a function of temperature for different oxygen contents[44].

The melt pools observed in this work remain shallow, which aligns with the behaviour associated with a negative $d\sigma/dT$. The referenced surface-tension gradient therefore supports that under the present processing conditions, it was unlikely to reverse the Marangoni flow direction.

Overall, whether a pore is able to escape or becomes trapped depends on the interaction between the Marangoni flow and the buoyancy forces, as well as the solidification. These flow mechanisms provide a basis for interpreting the porosity trends observed in the deposited thin-wall samples in this study.

During multi-layer deposition, remelting of the previous layer provides an additional opportunity for pores located near the previous solidification front to re-enter the liquid phase, and further move upward and escape. However, pores that cannot escape the melt pool are trapped.

- **Potential Sources for Porosity**
  As discussed in Chapter 2, hydrogen is considered the most likely source of gas pores in the LDED processes of aluminium alloys. Hydrogen exhibits significantly higher solubility in liquid metal compared to solid metal, resulting in supersaturation and thus the formation of vapour pores during solidification. Dissolved hydrogen may originate from the wire feedstock, and once pores nucleate, they can only be removed if they migrate to the melt pool surface before solidification.

  The shielding gas may also contribute to pore formation if argon becomes entrained in the melt pool. Argon has lower solubility in molten alloys and cannot dissolve back into the liquid metal, suggesting that the entrapment of argon is also possible, although it is considered less dominant than hydrogen-related pore formation.

Evaporation of alloying elements has been reported as a possible source of gas pores in the literature as well. However, the EDS results on compositional changes obtained in this work do not show strong evidence of loss of the alloying element in the thin-wall samples. Therefore, alloy evaporation is unlikely to have significantly contributed to pore formation under the conditions in this work.

- **Cleaning Procedure between Depositions**
  The cleaning between each pass during the multi-layer depositions may lead to a higher possibility of porosity. Considering that porosity is rarely found in single-bead deposition, as well as the tendency of pores to distribute along the interlayer regions in thin-wall samples, the cleaning between each layer of deposition might contribute to the pore formation.

  Although the deposited surface was brushed between layers, this procedure may leave oxide residues due to the not perfectly smooth surface, creating conditions that potentially introduce porosity. The present work does not directly investigate oxide presence or behaviour, but oxide-related mechanisms cannot be excluded and may represent an additional contributing factor. This is noted as a potential influence rather than a cause.

- **The Effect of Layer Number and Travel Speed**
  The porosity ratio was found to increase with the number of deposited layers. This behaviour can be linked to the thermal conditions that develop as the building height increases. With each subsequent layer, heat accumulates within the structure, and the increase in porosity with build height is consistent with repeated remelting and solidification between layers.

  Comparing the porosity ratios from two sets of thin-walls with different travel speeds, the set with a lower travel speed corresponded to a lower porosity. The escape of the pores is related to the solidification rate. Lower travel speed produces a larger and longer-lasting melt pool due to higher heat input per unit length. This provides more time for gas pores to float and escape prior to solidification. With a lower travel speed, it is more likely to allow gas to escape before solidification due to longer melt-pool lifetimes. In contrast, a higher travel speed shortens melt pool duration, which limits the time available for pore migration and increases the likelihood of entrapment.

- **Pore Distribution and Local Variation**
  The pores observed in cross-sections were shown to accumulate around the region between the layers. This distribution can be explained by the upward migration of pores toward the upper region of the melt pool under the influence of the Marangoni convection and the buoyancy effect. The pores tend to accumulate at the surface of the melt pool because the solidification of the melt pool tends to initiate from the bottom to top due to the bottom area's contact with the bulk material, which provides a relatively higher thermal conductivity[43]. Therefore, the pores eventually remain near the top surface in the melt pool before the full solidification is completed. As solidification proceeds, pores near the melt pool surface become trapped along the interface between layers, forming characteristic pore bands.

  In the previous work done by other researchers[45] [28], many found a similar distribution in the interlayer area, which leads to anisotropic properties in the material, further compromising their performance. However, it was reported in recent studies that there are effective methods that can improve the occurrence of porosity, by vibration-assisted systems.

  Among multiple cross-sections taken from the same thin-wall sample, a variation in porosity ratio was observed between different cross-sections taken from the same sample. This suggests that the porosity distribution may vary locally within the same thin-wall in the longitudinal direction, rather than being uniform across its length. Slight changes in the stability or surface roughness can locally alter melt pool dynamics and thus the pore formation.

  Since the cross-sections analysed in this work were taken from a single orientation, the present work cannot characterise the full three-dimensional distribution of pores. Further investigation would be required to determine the extent of spatial variability.

  Overall, the observed local variation does not contradict the general trends relating porosity to layer number and travel speed.

5.2.5 Hardness Test Analysis

The hardness profile along the thin-wall height shows an observable increase in hardness near the substrate, followed by a relatively constant hardness in the subsequent layers. This behaviour corresponds with the microstructural observations from EBSD. In the bottom section EBSD scan of TW 3, near the fusion line, the

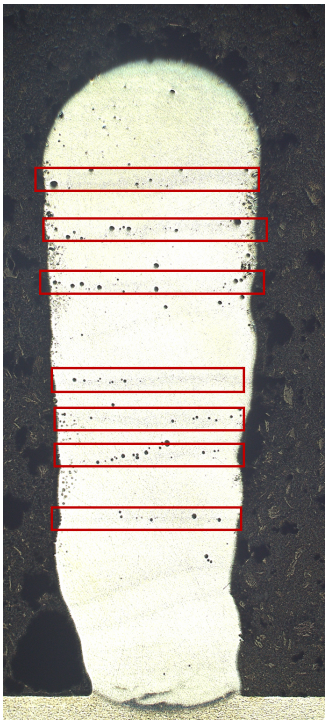

Figure 5.4: The distribution of the pores in a 12-layer thin-wall sample. (Interlayer regions with bands formed with pores are marked with red boxes.)

cooling rate is highest due to the thermal conductivity of the substrate, resulting in fine, equiaxed grains that contribute to the higher hardness in this region.

Moving away from the substrate, the EBSD maps show a gradual increase in grain size and the development of grains aligned with the build direction, consistent with directional solidification under a more stable thermal gradient. These microstructural changes explain why the hardness measurements lower and remain consistent after the initial layers.

Overall, the hardness results indicate that once the early layers are established, the thermal conditions during deposition become steady enough to produce a uniform microstructure and mechanical response.

5.2.6 Thermal Analysis

- **The Evolution of Heating and Cooling Rates**
  - **Heating Rates**
    Cycle 1 shows a lower heating rate for both thermocouples compared to Cycle 2. This is due to the initially colder substrate, acting as a heat sink during the first deposition. A portion of the supplied energy was thus consumed in order to heat up the substrate from room temperature to an elevated temperature, which in turn reduced the heating rate.

    From cycle 2 onward, the substrate and surrounding material were no longer at ambient temperature. As a result, less energy was required to raise the local temperature, and the heating rates increased. The highest heating rates occurred in cycle 2, followed by a gradual decrease. This decrease is related to the accumulation of material during the multi-layer build. Each newly deposited layer increases the thermal mass of the system and introduces additional thermal resistance, both of which reduce the efficiency of heat transfer. Consequently, progressively lower heating rates were measured in the later cycles.
  - **Cooling Rates**
    Unlike the heating rates, the cooling rates did not display a clear trend with increasing layer number. This can be explained by the nature of the cooling mechanism, related to the dominant convection and radiation. Cooling is primarily governed by heat loss to the surrounding environment. The measured cooling rates reflect primarily the external heat loss conditions, which remained consistent across all cycles. This explains the relatively constant cooling rates obtained for both thermocouples.

Other than the overall behaviour observed in cooling rates. Specifically, Thermocouple 1 consistently recorded higher cooling rates than Thermocouple 2, reflecting its higher peak temperatures and stronger thermal gradients.

- **Heat Accumulation**
  The progressive decrease in heating rates and peak temperatures indicates that heat accumulation occurred during the multilayer deposition. Although the measured pre-heating temperature increased only moderately, the thermal behaviour of the system changed more substantially. This is because heat accumulation in a multi-layer build does not depend solely on the absolute temperature but also on the evolving thermal resistance and heat capacity of the additional deposit.

  Each newly deposited layer gives an additional thermal conduction path between the heat source and the substrate. As a result, the efficiency of heat conduction into the substrate decreases progressively with higher layer numbers. At the same time, the accumulated layers store thermal energy, increasing the overall thermal mass and reducing the responsiveness of the system to heating.

  Taken various aspects into consideration collectively, these effects are consistent with the observed monotonic reduction in peak temperature and heating rate from cycle 2 to cycle 5.

- **Implications for Multi-layer Depositions**
  The observed trends in heating and cooling behaviour highlight the evolving thermal environment during multilayer deposition. Heat accumulation influences not only the maximum temperatures reached, but also the heating and cooling rate. Each subsequent layer responds to the deposition heat source. These changes may influence melt pool stability, local distortion, and interlayer bonding uniformity, which should be considered when analysing microstructural development and final part quality. Although finite-element thermal modelling was outside the scope of this work, the measured data provide valuable insight into the thermal evolution and its potential implications for process stability.

5.2.7 XRD Analysis

- **Peak Positioning and Lattice Parameter Deviations**
  The diffraction peaks observed in the XRD pattern exhibit slight shifts toward lower 2θ values compared with the reference positions of Al. This trend is reflected in the calculated d-spacing values and thus the lattice parameters, which are slightly larger than the reference value for pure aluminium ($a_{ref} \approx 4.049$ Å).

  Such deviations in lattice parameter can be attributed to the dissolution of Mg in the Al matrix, since Mg has a larger atomic size relative to Al. It was reported that in AI-Mg alloys, dissolved Mg atoms increase the Al-rich phase lattice parameter. For Mg contents higher than 2 at.% Mg, a linear increase of lattice expansion in the Al-rich phase can be observed[46].

  Alternatively, the peak shifts towards lower 2θ may arise from residual stress induced by the thermal gradients or sample preparation related to the process of LDED. In LDED processes, thermal gradients and repeated thermal cycles of previously deposited layers generate residual stresses that can affect the derived a-value. Moreover, it was reported that mechanical processing, such as grinding and machining, will also introduce additional surface residual stresses into the sample measured[47]. Such mechanical methods were conducted when the sample was being prepared for characterisation, thus it can also be affected by them.

  Overall, the measured deviations in lattice parameter may arise from both Mg partially in solid solution and from residual tensile stress in the deposit. These contributions cannot be separated uniquely from the present plotted diffractogram without further measurements.

- **Absence of Detectable Al_3Mg_2 Peaks in This Study**
  Despite the presence of Mg in the alloy, no distinct diffraction peaks corresponding to Al_3Mg_2 could be identified in the XRD pattern. Although the Al-Mg phase diagram indicates that Al_3Mg_2 can form at relevant compositions, its formation is dependent on the time and temperature. Intermetallic growth usually lies in solute diffusion and time at elevated temperature. Typically, the dissolved alloying elements exceed the solubility at room temperature, and they are kept in solid solution during cooling, leading to their supersaturation of the base material[48]. Rapid solidification process in LDED can result in Mg in supersaturated Al instead of the formation of Al_3Mg_2 precipitation. Therefore, even for alloys with a Mg content of ≈5 wt%, the intermetallic phase might be absent.

Furthermore, Al_3Mg_2 exhibits several reflections that lie close to dominant Al peaks, making them difficult to resolve when present at low volume fractions. Therefore, the absence of intermetallic peaks does not confirm the absence of Al_3Mg_2, but rather that under the present processing conditions, any such phase is rather non-detectable or masked by the aluminium matrix reflections.

- **Comparison with the Literature**
  The XRD pattern obtained from the deposited sample showed a set of diffraction peaks, and the distribution is consistent with those reported in previous studies using both LDED and WAAM of Al-Mg alloys. However, despite the similarity in the overall pattern, the identification of peaks reported in the literature varies among different studies. For instance, several authors have assigned selected peaks to the presence of intermetallic Al_3Mg_2, while others have identified the same reflections as belonging to the Al. Examples of such diffraction patterns from the literature are shown in Figure 5.5, each subfigure (b) – (e) shows the authors' assigned peak positions and reported identification of possible Al_3Mg_2 peaks. These variations illustrate the inconsistency in peak assignment across studies.

  There are potential explanations for why some authors detect or identify Al_3Mg_2 peaks while they are not distinguishable in the present work:

  To begin with, differences exist in the process of WAAM and LDED, resulting in different cooling rates and solidification processes. Besides the differences in the process, Al_3Mg_2 can present weak and undetectable reflections if the volume fraction is low. Moreover, Al_3Mg_2 has a complex structure with numerous weak reflections distributed across the diffraction plot. Some of these fall close to intense Al peaks, making them indistinguishable unless Al_3Mg_2 is abundant.

  The lack of agreement in peak attribution highlights the difficulty of distinguishing Al_3Mg_2 solely through XRD when its reflections overlap with those of aluminium.

- **Complexity of Al_3Mg_2**
  To further understand these observations, Figure 5.6 (b) presents a reference XRD pattern of Al_3Mg_2 reported in the literature. In the plot, the Al_3Mg_2 phase exhibits numerous low-intensity reflections and peaks at high (hkl) indices. The complexity of Al_3Mg_2 further complicates its identification. The phase exhibits a large number of crystallographic planes producing reflections within the 30–70° 2θ range, resulting in a dense cluster of peaks with relatively low intensity. When compared with the measured diffraction data in the present study, no systematic alignment with these characteristic reflections is observed. Given the degree of peak overlap and the low scattering contrast between Al and Mg, XRD alone is insufficient to unambiguously verify the presence of Al_3Mg_2 in the produced material. Techniques such as EBSD phase mapping or high-resolution diffraction would be required to confirm or exclude the phase with certainty. Therefore, based on the available evidence, the microstructure is best interpreted as an Al-rich solid solution without detectable intermetallic formation.

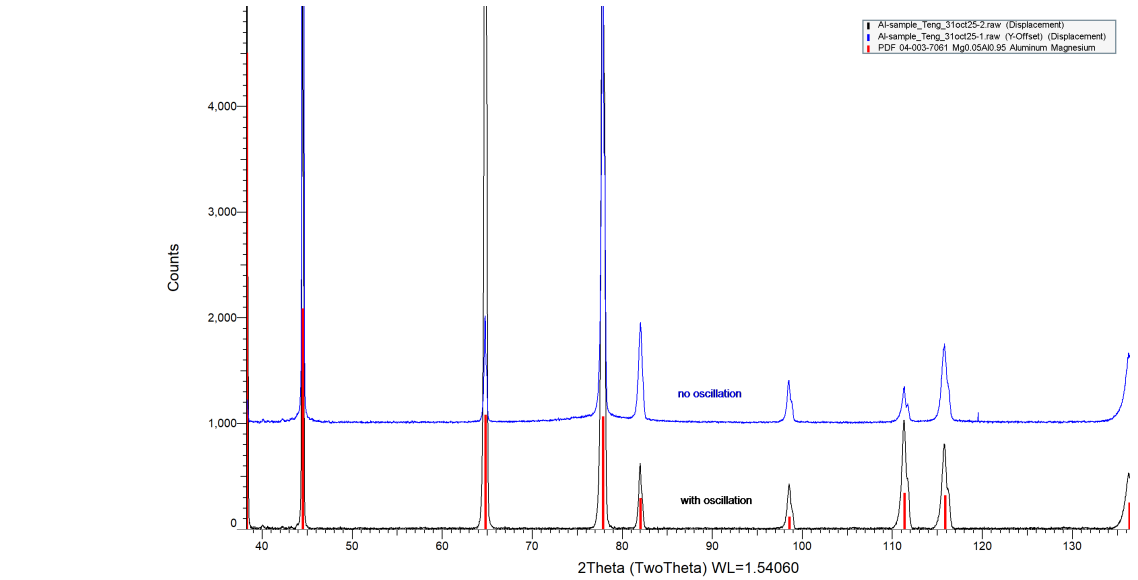

(a) XRD diffraction peak profile of the thin-wall sample (TW3) in this work.

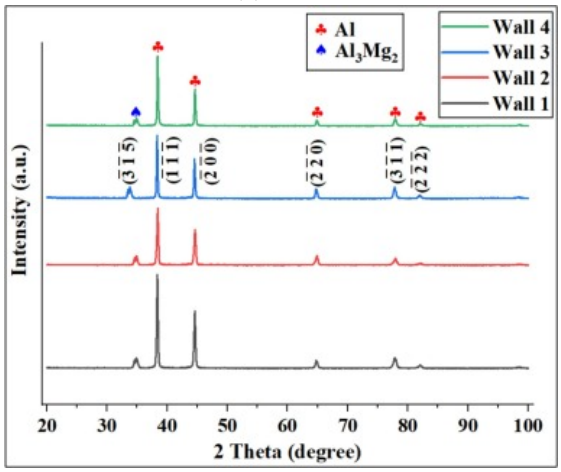

(b) J. Singla, 2024[16].

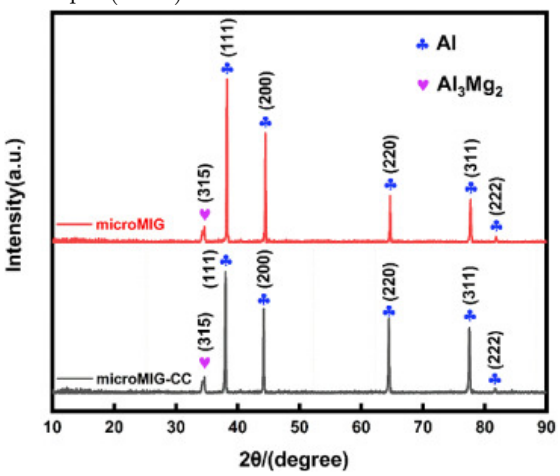

(c) P. Jiangang, 2022[49].

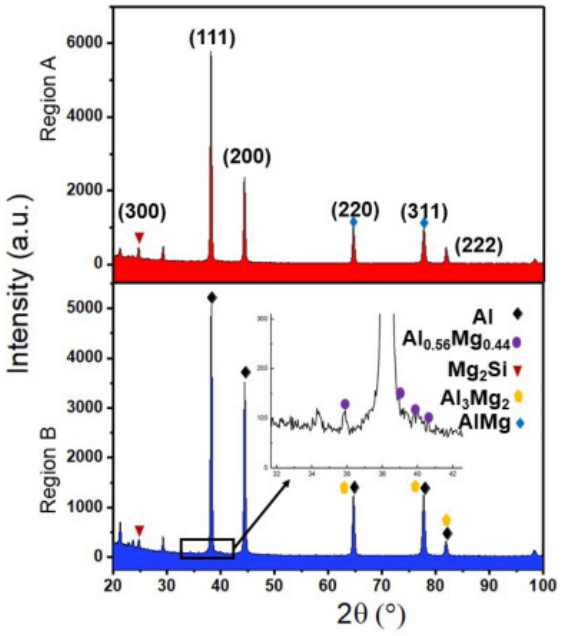

(d) Y. Geng, 2022[50].

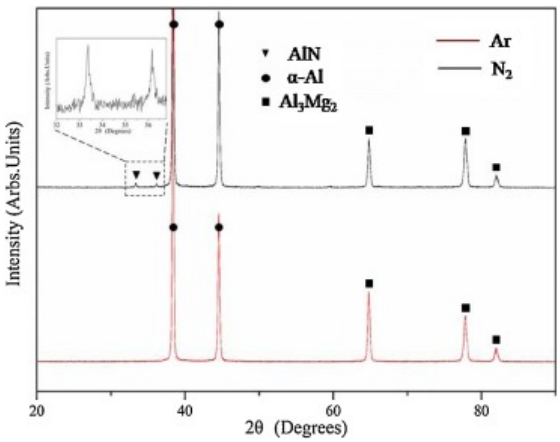

(e) S. Li, 2020[51].

Figure 5.5: Comparison of XRD peak profiles reported in the literature for additively manufactured Al–Mg alloys.

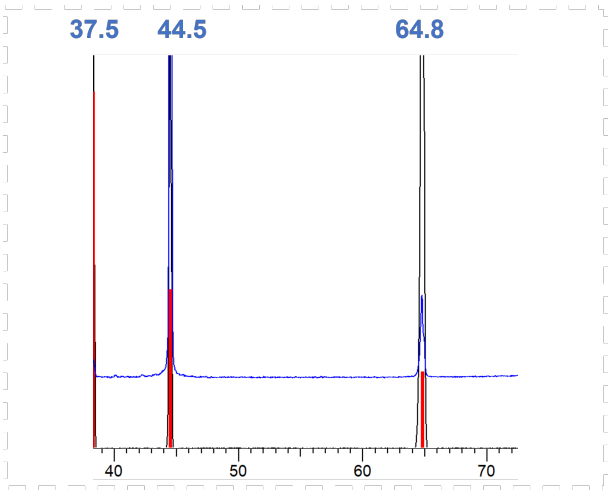

(a) Cropped plot of XRD diffraction peak profile from the present work

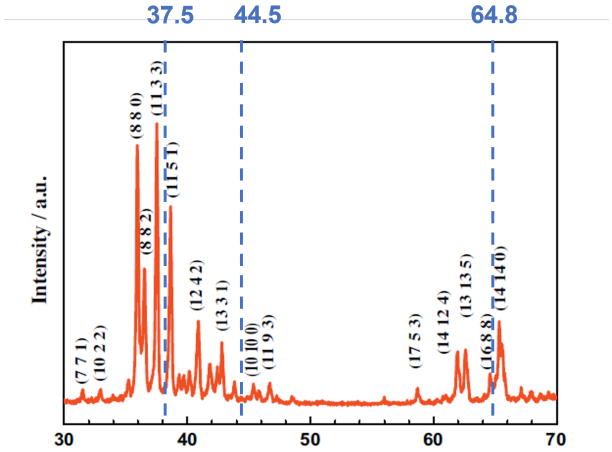

(b) XRD diffraction peak profile for synthesised Al_3Mg_2 [52]

Figure 5.6: Overlay of the present XRD peak profile (cropped to 37–70° 2θ) and the reference pattern for synthesised Al_3Mg_2 from Guan, 2016[52]. The dashed lines mark the 2θ positions from the present work for comparison.

Chapter 6

Conclusions and Recommendations

6.1 Conclusions

From the results and discussions included in this study, the following conclusions arise, which will be discussed in two stages:

6.1.1 Single-Bead Depositions

- Key process parameters (laser power, travel speed, wire-feeding rate) studied primarily influenced bead geometry. Geometry trends followed a predictable logic between the heat input and the amount of the feedstock being fed. Despite that the results did not yield a single "optimal" condition, as the inherent multi-variable trade-offs exist in the single-bead deposition results, a workable parameter window for further vertical depositions is developed.
- Single-bead tracks do not develop the clear columnar/equiaxed transitions seen in multi-layer builds. However, the main microstructural outcome observed across single-bead depositions is linked to compositional variation, suggesting a mixing or dilution with the substrate.

6.1.2 Multi-Layer Depositions

- Thin-wall shape evolution was affected by initiation/termination instability and first-layer geometry, leading to the observed shift from thin-to-thick walls.
- The microstructure evolution followed the patterns typical of DED processes, with columnar grains forming under large thermal gradients and finer equiaxed dendrites appearing in regions with higher cooling. The reproducibility of these features across builds suggests that the thermal conditions remained stable throughout the experiments. While microstructure tailoring was not attempted in this study, the consistency of the observed features aligns with previous work, indicating that microstructure control in LDED is achievable through thermal management.
- Distortion increased with the number of layers, reflecting the cumulative thermal cycles inherent to multi-layer LDED. Higher heat input conditions resulted in a larger melt pool and a greater volume of material is affected, which in turn contributed to increased warpage. These observations align with the general understanding that energy input influences thermal accumulation and thereby affects distortion behaviour.
- Porosity increased with both layer number and travel speed. These trends align with the shorter melt pool lifetime at higher speeds, which limits the time for gas bubbles to escape before solidification. The pore morphology indicates the pores are gas-driven, which aligns with mechanisms commonly reported in AM processes, such as hydrogen and shielding gas entrapment. Compositional analysis in this work did not reveal measurable magnesium loss, making Mg evaporation a less likely contributor. Therefore, hydrogen from the feedstock is considered the most plausible primary source, although alternative gas entrapment mechanisms cannot be excluded. The observed cluster of pores at interlayer regions and the lack of observed porosity in single-bead depositions further suggest that the cleaning process may have influenced the distribution, highlighting the sensitivity of pore formation to surface state.

6.2 Recommendations

On the basis of the present study, some recommendations to further improve the results obtained and the possibilities can be explored for further research:

- **Enhance initiation–termination synchronisation**
  The irregularities observed at track start and stop indicate sensitivity to the coordination between the wire-feeder and the worktable. Transitioning to automated synchronisation could ensure a more consistent melt pool at the start and stabilise the deposition during critical moments. Improving the consistency would reduce geometric accumulation effects in multi-layer builds and contribute to more uniform wall formation in future experiments.

- **Improved cleaning process between depositions**
  The distribution of porosity suggests that more standardised cleaning procedures between multi-layer deposition would be beneficial. Implementing controlled surface preparation, such as sufficient cleaning to minimise surface oxides or moisture, could reduce the porosity introduced during each layer. Establishing a repeatable cleaning workflow would help isolate feedstock-related effects from operator-induced variability and allow future studies to better assess the intrinsic porosity behaviour of the process.

- **Multi-pass deposition experiments to study inter-track defect evolution**
  The current work focuses on single-track multi-layer wall builds, but many industrial applications require multi-pass strategies. Introducing overlapping tracks would enable examination of defect mechanisms. Understanding how horizontally-overlapped tracks influence local thermal cycles, distortion development, and pore migration would provide important insight for practical build strategies.

- **Compare wire-based LDED with powder-based DED for cross-process validation**
  Since wire-based and powder-based DED systems differ in melt pool dynamics and the interaction between the heat source and the feedstock, a comparative study could clarify which thermal and defect trends are specific to wire deposition versus general to all DED processes. This would help contextualise the behaviour observed in this thesis within the broader AM field and improve the transferability of findings to different industrial setups.

- **Thermal modelling to link process parameters to microstructure and distortion**
  Thermal simulations could provide predictive information on temperature gradients, cooling rates and bead geometry. Such modelling would allow future studies to anticipate solidification behaviour, grain growth, and distortion development, facilitating more informed parameter optimisation. Integration of modelled and experimental thermal fields would also improve the interpretations of relationships between the process and defect control.

- **Melt pool fluid-flow modelling to analyse pore formation and remelting mechanisms**
  Modelling the melt pool fluid dynamics would complement thermal simulations by revealing how convection currents influence pore migration, gas escape, and remelting behaviour between each deposition. A combined thermal–fluid approach would support a more comprehensive understanding of pore entrapment and provide a framework for evaluating strategies aimed at reducing porosity.

Bibliography

[1] T. Liu et al. "Review on laser directed energy deposited aluminum alloys". In: *International Journal of Extreme Manufacturing* 6 (2 2024), p. 022004. DOI: 10.1088/2631-7990/ad16bb.

[2] J. Cheng et al. "An overview of laser metal deposition for cladding: defect formation mechanisms, defect suppression methods and performance improvements of laser-cladded layers". In: *Materials* 15 (16 2022), p. 5522. DOI: 10.3390/ma15165522.

[3] C. Selcuk. "Laser metal deposition for powder metallurgy parts". In: *Powder Metallurgy* 54 (2 2011), pp. 94–99. DOI: 10.1179/174329011x12977874589924.

[4] N. Shamsaei et al. "An overview of direct laser deposition for additive manufacturing; part ii: mechanical behavior, process parameter optimization and control". In: *Additive Manufacturing* 8 (2015), pp. 12–35. DOI: 10.1016/j.addma.2015.07.002.

[5] T. Wang et al. "Grain morphology evolution behavior of titanium alloy components during laser melting deposition additive manufacturing". In: *Journal of Alloys and Compounds* 632 (2015), pp. 505–513. DOI: 10.1016/j.jallcom.2015.01.256.

[6] M. Abuabiah et al. "Advancements in laser wire-feed metal additive manufacturing: a brief review". In: *Materials* 16 (5 2023), p. 2030. DOI: 10.3390/ma16052030.

[7] W. U. H. Syed, A. J. Pinkerton, and L. Li. "Combining wire and coaxial powder feeding in laser direct metal deposition for rapid prototyping". In: *Applied Surface Science* 252 (13 2006), pp. 4803–4808. DOI: 10.1016/j.apsusc.2005.08.118.

[8] T. Sibisi et al. "Lam additive manufacturing: a fundamental review on mechanical properties, common defects, dominant processing variables, and its applications". In: *The International Journal of Advanced Manufacturing Technology* 128 (7-8 2023), pp. 2847–2861. DOI: 10.1007/s00170-023-12139-w.

[9] R. Indhu et al. "Overview of laser absorptivity measurement techniques for material processing". In: *Lasers in Manufacturing and Materials Processing* 5 (4 2018), pp. 458–481. DOI: 10.1007/s40516-018-0075-1.

[10] T. Hassel, A. Beniyash, and G. Klimov. "Non-vacuum electron beam welding and cutting of cupper". In: *IOP Conference Series: Materials Science and Engineering* 759 (1 2020), p. 012003. DOI: 10.1088/1757-899x/759/1/012003.

[11] J. Svenungsson, I. Choquet, and A. Kaplan. "Laser welding process – a review of keyhole welding modelling". In: *Physics Procedia* 78 (2015), pp. 182–191. DOI: 10.1016/j.phpro.2015.11.042.

[12] M. Balbaa et al. "On selective laser melting of inconel 718: densification, surface roughness, and residual stresses". In: *Materials Amp; Design* 193 (2020), p. 108818. DOI: 10.1016/j.matdes.2020.108818.

[13] W. Gao et al. "Effect of defocus manner on laser cladding of fe-based alloy powder". In: *Surface and Coatings Technology* 248 (2014), pp. 54–62. DOI: 10.1016/j.surfcoat.2014.03.019.

[14] H. Fan et al. "A review of laser additive manufacturing (lam) aluminum alloys: methods, microstructures and mechanical properties". In: *Optics Amp; Laser Technology* 175 (2024), p. 110722. DOI: 10.1016/j.optlastec.2024.110722.

[15] G. Langelandsvik et al. "Review of aluminum alloy development for wire arc additive manufacturing". In: *Materials* 14 (18 2021), p. 5370. DOI: 10.3390/ma14185370.

[16] J. Singla, N. Kumar, and A. Bansal. "Microstructural and mechanical properties of al-5356 alloy structures fabricated using direct energy deposition (ded): in-pursuit to optimizing deposition parameters". In: *Materials Characterization* 216 (2024), p. 114321. DOI: 10.1016/j.matchar.2024.114321.

[17] A. M. Rubenchik et al. "Temperature-dependent 780-nm laser absorption by engineering grade aluminum, titanium, and steel alloy surfaces". In: *Optical Engineering* 53 (12 2014), p. 122506. DOI: 10.1117/1.oe.53.12.122506.

[18] Y. Yan et al. “Experimental and theoretical investigation of fibre laser crack-free cutting of thick-section alumina”. In: *International Journal of Machine Tools and Manufacture* 51 (12 2011), pp. 859–870. DOI: 10.1016/j.ijmachtools.2011.08.004.

[19] A. D. Silva et al. “Influence of aluminium powder aging on directed energy deposition”. In: *Materials Amp; Design* 218 (2022), p. 110677. DOI: 10.1016/j.matdes.2022.110677.

[20] H. Wei et al. “Mechanistic models for additive manufacturing of metallic components”. In: *Progress in Materials Science* 116 (2021), p. 100703. DOI: 10.1016/j.pmatsci.2020.100703.

[21] H. Zhao and T. DebRoy. “Weld metal composition change during conduction mode laser welding of aluminum alloy 5182”. In: *Metallurgical and Materials Transactions B* 32 (1 2001), pp. 163–172. DOI: 10.1007/s11663-001-0018-6.

[22] X. Lu et al. “Residual stress and distortion of rectangular and s-shaped ti-6al-4v parts by directed energy deposition: modelling and experimental calibration”. In: *Additive Manufacturing* 26 (2019), pp. 166–179. DOI: 10.1016/j.addma.2019.02.001.

[23] G. Piscopo et al. “An overview of the process mechanisms in the laser powder directed energy deposition”. In: *Applied Sciences* 13 (1 2022), p. 117. DOI: 10.3390/app13010117.

[24] E. Yasa et al. “A study on the stair stepping effect in direct metal laser sintering of a nickel-based superalloy”. In: *Procedia CIRP* 45 (2016), pp. 175–178. DOI: 10.1016/j.procir.2016.02.068.

[25] M. Froend et al. “Process development for wire-based laser metal deposition of 5087 aluminium alloy by using fibre laser”. In: *Journal of Manufacturing Processes* 34 (2018), pp. 721–732. DOI: 10.1016/j.jmapro.2018.06.033.

[26] T. Hauser et al. “Porosity in wire arc additive manufacturing of aluminium alloys”. In: *Additive Manufacturing* 41 (2021), p. 101993. DOI: 10.1016/j.addma.2021.101993.

[27] A. P. Boeira, I. L. Ferreira, and A. Garcia. “Alloy composition and metal/mold heat transfer efficiency affecting inverse segregation and porosity of as-cast al–cu alloys”. In: *Materials Design* 30 (6 2009), pp. 2090–2098. DOI: 10.1016/j.matdes.2008.08.032.

[28] Jianglong Gu et al. *Wire+ arc additive manufacturing of aluminum*. 2014.

[29] B. C. D. Borges et al. “Imperfections in laser clading with powder and wire fillers”. In: *The International Journal of Advanced Manufacturing Technology* 50 (1-4 2009), pp. 175–183. DOI: 10.1007/s00170-009-2480-2.

[30] K. Moeinfar et al. “A review on metallurgical aspects of laser additive manufacturing (lam): stainless steels, nickel superalloys, and titanium alloys”. In: *Journal of Materials Research and Technology* 16 (2022), pp. 1029–1068. DOI: 10.1016/j.jmrt.2021.12.039.

[31] D. Svetlizky et al. “Directed energy deposition (ded) additive manufacturing: physical characteristics, defects, challenges and applications”. In: *Materials Today* 49 (2021), pp. 271–295. DOI: 10.1016/j.mattod.2021.03.020.

[32] J. Fu et al. “Multi-scale defects in powder-based additively manufactured metals and alloys”. In: *Journal of Materials Science Amp; Technology* 122 (2022), pp. 165–199. DOI: 10.1016/j.jmst.2022.02.015.

[33] D. Y. Pimenov et al. “Influence of selective laser melting process parameters on the surface integrity of difficult-to-cut alloys: comprehensive review and future prospects”. In: *The International Journal of Advanced Manufacturing Technology* 127 (3-4 2023), pp. 1071–1102. DOI: 10.1007/s00170-023-11541-8.

[34] Weiwei Liu et al. “Evolution of melt pool motion and temperature field based on powder scale modeling during laser directed energy deposition process”. In: *Applied Thermal Engineering* 243 (2024), p. 122564. ISSN: 1359-4311. DOI: https://doi.org/10.1016/j.applthermaleng.2024.122564.

[35] A. Ebrahimi et al. “Revealing the effects of laser beam shaping on melt pool behaviour in conduction-mode laser melting”. In: *Journal of Materials Research and Technology* 27 (2023), pp. 3955–3967. DOI: 10.1016/j.jmrt.2023.11.046.

[36] Sindo Kou. “Welding metallurgy”. In: *New Jersey, USA* 431.446 (2003), pp. 223–225.

[37] H. Wei, J. W. Elmer, and T. DebRoy. “Origin of grain orientation during solidification of an aluminum alloy”. In: *Acta Materialia* 115 (2016), pp. 123–131. DOI: 10.1016/j.actamat.2016.05.057.

[38] M. Gäumann et al. “Epitaxial laser metal forming: analysis of microstructure formation”. In: *Materials Science and Engineering: A* 271 (1-2 1999), pp. 232–241. DOI: 10.1016/s0921-5093(99)00202-6.

[39] T. DebRoy et al. "Additive manufacturing of metallic components – Process, structure and properties". In: *Progress in Materials Science* 92 (2018), pp. 112–224. ISSN: 0079-6425. DOI: https://doi.org/10.1016/j.pmatsci.2017.10.001.

[40] A. Heralić et al. "Control design for automation of robotized laser metal-wire deposition". In: *IFAC Proceedings Volumes* 41 (2 2008), pp. 14785–14791. DOI: 10.3182/20080706-5-kr-1001.02503.

[41] A. Zapata et al. "Investigation on the cause-effect relationships between the process parameters and the resulting geometric properties for wire-based coaxial laser metal deposition". In: *Metals* 12 (3 2022), p. 455. DOI: 10.3390/met12030455.

[42] N. Ghanadi and S. Pasebani. "A review on wire-laser directed energy deposition: parameter control, process stability, and future research paths". In: *Journal of Manufacturing and Materials Processing* 8 (2 2024), p. 84. DOI: 10.3390/jmmp8020084.

[43] G. Yu et al. "Influence of processing parameters on laser penetration depth and melting/re-melting densification during selective laser melting of aluminum alloy". In: *Applied Physics A* 122 (10 2016). DOI: 10.1007/s00339-016-0428-6.

[44] A. E. Gheribi and P. Chartrand. "Temperature and oxygen adsorption coupling effects upon the surface tension of liquid metals". In: *Scientific Reports* 9 (1 2019). DOI: 10.1038/s41598-019-43500-3.

[45] M. Gierth et al. "Wire arc additive manufacturing (waam) of aluminum alloy almg5mn with energy-reduced gas metal arc welding (gmaw)". In: *Materials* 13 (12 2020), p. 2671. DOI: 10.3390/ma13122671.

[46] V. K. Singh et al. "Electronic structure of al3mg2 and al13fe4<". In: *Physical Review B* 105 (20 2022). DOI: 10.1103/physrevb.105.205107.

[47] Michael Fitzpatrick et al. *NPL Good Practice Guide no. 52: determination of residual stresses by x-ray diffraction*. Jan. 2002.

[48] B. Milkereit et al. "Review of the quench sensitivity of aluminium alloys: analysis of the kinetics and nature of quench-induced precipitation". In: *Materials* 12 (24 2019), p. 4083. DOI: 10.3390/ma12244083.

[49] P. jiangang et al. "Influence of arc mode on the microstructure and mechanical properties of 5356 aluminum alloy fabricated by wire arc additive manufacturing". In: *Journal of Materials Research and Technology* 20 (2022), pp. 1893–1907. DOI: 10.1016/j.jmrt.2022.08.005.

[50] Y. Geng et al. "Wire arc additive manufacturing al-5.0 mg alloy: microstructures and phase composition". In: *Materials Characterization* 187 (2022), p. 111875. DOI: 10.1016/j.matchar.2022.111875.

[51] S. Li et al. "Comparative study on the microstructures and properties of wire+arc additively manufactured 5356 aluminium alloy with argon and nitrogen as the shielding gas". In: *Additive Manufacturing* 34 (2020), p. 101206. DOI: 10.1016/j.addma.2020.101206.

[52] L. Guan et al. "Influence of aging treatment on the pitting behavior associated with the dissolution of active nanoscale -phase precipitates for an al–mg alloy". In: *Corrosion Science* 103 (2016), pp. 255–267. DOI: 10.1016/j.corsci.2015.11.026.